Dynamic stability of geosynthetic-reinforced soil integral bridge

H. Munoz[1], F. Tatsuoka[2], D. Hirakawa[3], H. Nishikiori[4], R. Soma[5], M. Tateyama[6] and K. Watanabe[7]

[1] *Research Engineer, Japan-Peru Centre for Earthquake Engineering Research and Mitigation of Disasters CISMID, National University of Engineering, Lima, Peru, Telephone and Telefax: +51 1 482 0804, E-mail: hmunoz22@yahoo.com; formerly Graduate Student, Department of Civil Engineering, Tokyo University of Science*

[2] *Professor, Department of Civil Engineering, Tokyo University of Science, 2641 Yamazaki, Noda, Chiba, 278-8510, Japan, Telephone: +81 4 7122 9819, Telefax: +81 4 7123 9766, E-mail: tatsuoka@rs.noda.tus.ac.jp*

[3] *Assistant Professor, Department of Civil and Environmental Engineering, National Defence Academy of Japan, 1-10-20 Hashirimizu, Yokosuka, Kanagawa, 239-8686, Japan, Telephone: +81 46 841 3810, Telefax: +81 46 844 5913, E-mail: hirakawa@nda.ac.jp*

[4] *Engineer, Department of Civil Engineering, Ibaraki Prefecture, 978-6 Kasahara, Mito City, Ibaraki Prefecture, Japan, Telephone: +81 29 301 4530, Telefax: +81 29 301 4538, E-mail: h.nishikiori@pref.ibaraki.lg.jp*

[5] *Civil Engineer, Piping and Civil Engineering Division, Toyo Engineering Corporation, 2-8-1 Akanehama, Narashino City, Chiba 275-0024, Japan, Telephone:+81 47 454 1656, Telefax:+81 47 454 1540, E-mail: soma-r@ga.toyo-eng.co.jp*

[6] *Chief, Structural Engineering Division, Railway Technical Research Institute, Japan, 2-8-38, Hikaricho, Kokubunji City, Tokyo, 185 8540, Japan, Telephone: +81 42 573 7369, Telefax: +81 42 053 7369, E-mail: tate@rtri.or.jp*

[7] *Assistant Senior Researcher, Foundation and Geotechnical Engineering Structures Technology Division, Railway Technical Research Institute, Japan, 2-8-38, Hikari-cho, Kokubunji City, Tokyo, 185-8540, Japan, Telephone: +81 42 573 7261, Telefax: +81 42 573 7248, E-mail: nabeken@rtri.or.jp*

ABSTRACT: To evaluate the dynamic stability of different bridge types, the results from a series of shaking-table tests on small-scale models of the following bridge types were analysed within the framework of the single-degree-of-freedom theory: (1) a conventional bridge (CB), comprising a girder (i.e. deck) supported via a pair of movable and fixed bearings (i.e. shoes) by gravity-type abutments (without a pile foundation) having unreinforced backfill; (2) a GRS-RW bridge, comprising a girder supported via a pair of movable and fixed bearings by a pair of sill beams placed on the crest of a pair of geosynthetic-reinforced soil-retaining walls (GRS-RWs) having a stage-constructed full-height rigid facing; (3) an integral bridge (IB), comprising a girder integrated to a pair of abutments (without bearings) and unreinforced backfill; (4) a GRS integral bridge, comprising a girder integrated to the abutments (in the same way as the IB bridge) while the backfill is reinforced with geosynthetic layers connected to the facings (in the same way as the GRS-RW bridge); and (5) a GRS integral bridge with a cement-mixed soil zone of rectangular prismatic or trapezoidal shape immediately behind the facing. The following is shown: the stability of the bridge against dynamic excitations increases: (1) with an increase in the initial natural frequency via an increase in the initial stiffness; (2) with a decrease in the decreasing rate of stiffness during cyclic loading (i.e. an increase in the dynamic ductility); (3) with an increase in the damping energy dissipation capacity near and at failure; and (4) with an increase in the dynamic strength. With the GRS integral bridge, the structural integration and geosynthetic-reinforcing of the backfill, as well as cement-mixing of the backfill immediately behind the facings, all contribute to the evolution of these four factors. The natural frequency can then always be kept much higher than the predominant frequency of ordinary design earthquake motion, the response acceleration is kept sufficiently low, and the dynamic stability can be kept very high.

KEYWORDS: Geosynthetics, Dynamic stability, Geosynthetic-reinforced soil, Integral bridge, Seismic design, Shaking table model tests

1. INTRODUCTION

A conventional bridge usually comprises a girder (i.e. a deck), simply supported by a pair of abutments via a pair of movable and fixed bearings (i.e. shoes), or multiple girders supported by a pair of abutments and a pier (or piers) via multiple sets of bearings that are connected with fixtures, while the backfill is not reinforced. Numerous conventional bridges have been seriously damaged (i.e. failed) or have totally collapsed during many previous earthquakes. Therefore there has been a pressing need to develop a new bridge type that is more earthquake-resistant yet more cost-effective. Tatsuoka *et al.* (2009) proposed a new type of bridge, called the geosynthetic-reinforced soil integral bridge (the GRS integral bridge), which comprises an integral bridge and geosynthetic-reinforced backfill (Figure 1).

Based on results from a series of model tests (i.e. static lateral cyclic loading tests and shaking-table tests) of the four different one-span bridge types shown in Figure 1, Tatsuoka *et al.* found the following trends of behaviour.

1. The integral bridge with unreinforced backfill may exhibit large settlement in the backfill, together with serious structural damage to the facing, owing to an increase in the lateral earth pressure caused by cyclic lateral displacements at the top of the facing from seasonal thermal cyclic expansion and contraction of the girder. By contrast, the GRS integral bridge is free from these problems.

2. In the conventional bridge, with the girder supported by a pair of abutments via fixed and movable bearings and unreinforced backfill, the seismic stability of both structural components (the pair of abutments and the girder) and the backfill is very low, because they are not integrated with each other. The integral bridge alleviates the problem with the structural components by removing the fixed and movable bearings. The geosynthetic-reinforced soil-

retaining wall bridge (GRS-RW bridge), with the girder supported via bearings at sill beams placed on the crest of the backfill, alleviates the problem with the backfill by reinforcing it with geogrid layers connected to the back of the full-height rigid (FHR) facing. By contrast, the GRS integral bridge has a very high seismic stability of both structural components (the girder and the pair of abutments) and backfill, because they are integrated with each other.

These characteristic features of the GRS integral bridge can be attributed to the following factors.

- Bearings are not used to support the girder.
- The girder is continuous.
- The backfill is reinforced with geogrid layers firmly connected to the FHR facing.
- FHR facings (i.e. bridge abutments) are stage-constructed after the construction of the full-height geosynthetic-reinforced backfill and pile foundations (if needed).

The pile foundations (if needed) are much lighter than those for conventional bridges and integral bridges. The GRS integral bridge is therefore highly cost-effective in construction and long-term maintenance, while remaining very stable under static and seismic loading conditions.

As a follow-up, the present study was performed to evaluate the dynamic stability of the four bridge types shown in Figure 1 by analysing the results from a series of shaking-table tests on small-scale models in the framework of the single-degree-of-freedom theory as an approximated and simplified but rational theoretical basis, aiming at use in ordinary design practice. The dynamic stability is defined in this study as the capability of a given structural system to exhibit stable dynamic behaviour without failure against given dynamic loads (such as seismic loads). The study examined whether the dynamic stability of the bridge increases with an increase not only in the dynamic strength, defined as the response acceleration at which the failure starts, but also in the initial stiffness, the dynamic ductility (i.e. the decreasing rate of the stiffness by dynamic loading), and the damping capacity (i.e. the capacity to dissipate the dynamic energy of the structural components). It also examined whether these features can be effectively achieved by structurally integrating the bridge girder abutments (i.e. the FHR facings) and reinforcing the backfill with geogrid layers connected to the back of the FHR facing. The effects of cement-mixing of part of the backfill immediately behind the FHR facings for the GRS integral bridge were also evaluated.
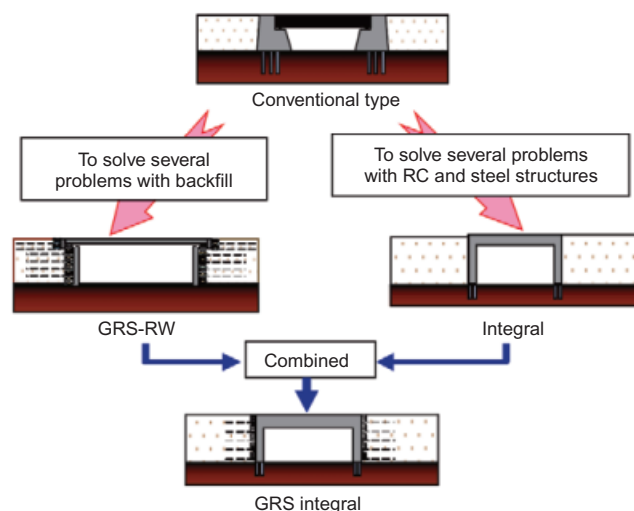
Figure 1. Development of new bridge type to alleviate technical problems of conventional bridges (not to scale) (Tatsuoka *et al.* 2009)

# 2. SHAKING-TABLE TESTS

2.1. General

As the details of the shaking-table tests are reported in Tatsuoka *et al.* (2009), only a brief summary is given below. In total, six different types of small-scale bridge

models, listed in Table 1 and described below (Figures 2–7), were constructed inside a rectangular prismatic steel box (205.8 cm long, 60 cm wide and 140 cm high) fixed to a shaking table. The front side of the box comprises a transparent-tempered glass window to observe the displacements and deformations of the model during the shaking-table tests (see pictures in Figures 11–14). The opposite side of the steel box comprises a steel plate covered with a 0.2 mm thick Teflon sheet to minimise the effect of wall friction in the tests. The models were designed assuming a scale-down factor in length (i.e. the ratio in length between the prototype and its small model), λ, equal to 10. That is, it was assumed that the model girder arranged 51 cm high above the ground level simulates an ordinary full-scale girder placed on the abutments at a height of 5.1 m from the ground surface. The test results of the first four types were reported by Tatsuoka *et al.* (2009); those of the last two, which have a cement-mixed sand zone of two different shapes immediately behind the FHR facings of the GRS integral bridge, are reported for the first time in this paper. For the last type (Figure 7), two models were produced to test using two different dynamic loading histories, so in total seven model tests were conducted.

2.2. Bridge models

2.2.1. *Conventional bridge (CB; Figure 2)*
This is a model of a one-span bridge comprising a pair of gravity-type abutments supporting a simply supported girder on their top via fixed and movable bearings with unreinforced backfill. The gravity-type abutments of this model (i.e. CB model and its spread-footing foundation, 59 cm long, 20 cm wide and 6 cm high), as well as the full-height rigid (FHR) facing (59 cm long, 5 cm wide and 45 cm high) of the other models explained below, were made of duralumin. The back faces of a pair of abutments, and those of the FHR facings of the other models, and the bottom surfaces of their foundations, were in direct contact with the backfill and supporting ground. Hence these surfaces were made rough by being covered with a sheet of sandpaper (No. 150). The fixed bearing (at the
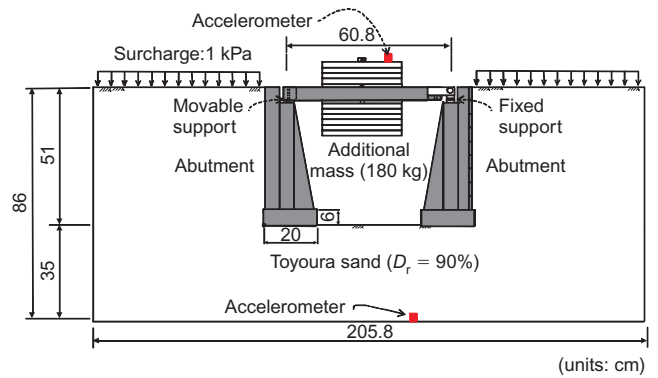
Figure 2. Conventional bridge model (only two accelerometers are indicated) (Tatsuoka *et al.* 2009)

right end of the girder in Figure 2) was allowed to rotate about a pin, while the movable bearing was allowed to slide horizontally on a linear rail. This CB model and the GRS-RW model (explained below) used bearings to support the girder. Hence they were asymmetric about the centre, which induced an asymmetric response against a symmetric sinusoidal input horizontal motion, as shown below.

The target length of the prototype girder for the tested bridge models was chosen to be equal to 20 m, which makes the length of the model girder equal to 2 m for a scale factor of $1/\lambda = 1/10$. Owing to the size constraint of the sand box, it was not possible to use a 2 m long model girder. Therefore a shorter one, 60.8 cm long, made of steel with a weight of 25 kg bearing an additional mass of 180 kg at its centre, was used. With this arrangement, the horizontal and vertical loads activated at the top of the abutments by the short girder model became identical to those in a 2 m long girder model.

The supporting ground and backfill were produced by pluviating air-dried Toyoura sand ($e_{max} = 0.970$, $e_{min} = 0.602$, $G_s = 2.65$, $U_c = 1.64$, $D_{50} = 0.179$ mm) to obtain a relative density D_r of about 90%. To observe the deformation of the backfill during the shaking tests, thin horizontal layers (with a width of about 1 cm) of Toyoura

Table 1. Initial natural frequencies and various physical quantities at start of failure of different bridge models subjected to sinusoidal base acceleration at $f_i = 5$ Hz

Bridge type	Initial natural frequency, f_0 (Hz)	Values at start of failure						
		Stage	(1) M_{peak} = (6)/(4)	(2) $\beta_{resonance}$	(3) $\xi_{resonance}$	(4) Amp$[\ddot{u}_b]_{resonance}$ (gal)[a]	(5) Max$[\ddot{u}_b]$ (gal)	(6) Strength = Amp$[\ddot{u}_t]_{resonance}$ (gal)
CB	11	III (5)[b]	1.85	0.97	0.33	214	228	397
		VII (6)[c]	1.43	0.91	0.52	635	659	906
GRS-RW	24	IV (4)	1.60	0.85	0.42	341	348	546
		VI (8)[c]	1.31	0.98	0.61	527	562	689
IB	25	VI (20)	1.61	0.87	0.42	520	547	838
GRS-IB	35	XI (7)	1.38	0.92	0.56	999	1036	1374
GRS-IB-C	35	XII (20)	1.33	0.86	0.62	1079	1126	1434
GRS-IB-C-T	35	XIII (4)	1.31	0.92	0.64	1150	1181	1502

[a]1 gal = 1 cm/s^2 = 0.01 m/s^2.
[b]Numbers in parentheses indicate number of cycles at each loading stage.
[c]Values of second resonance after end of girder has contacted abutment (or sill beam) at a movable bearing.
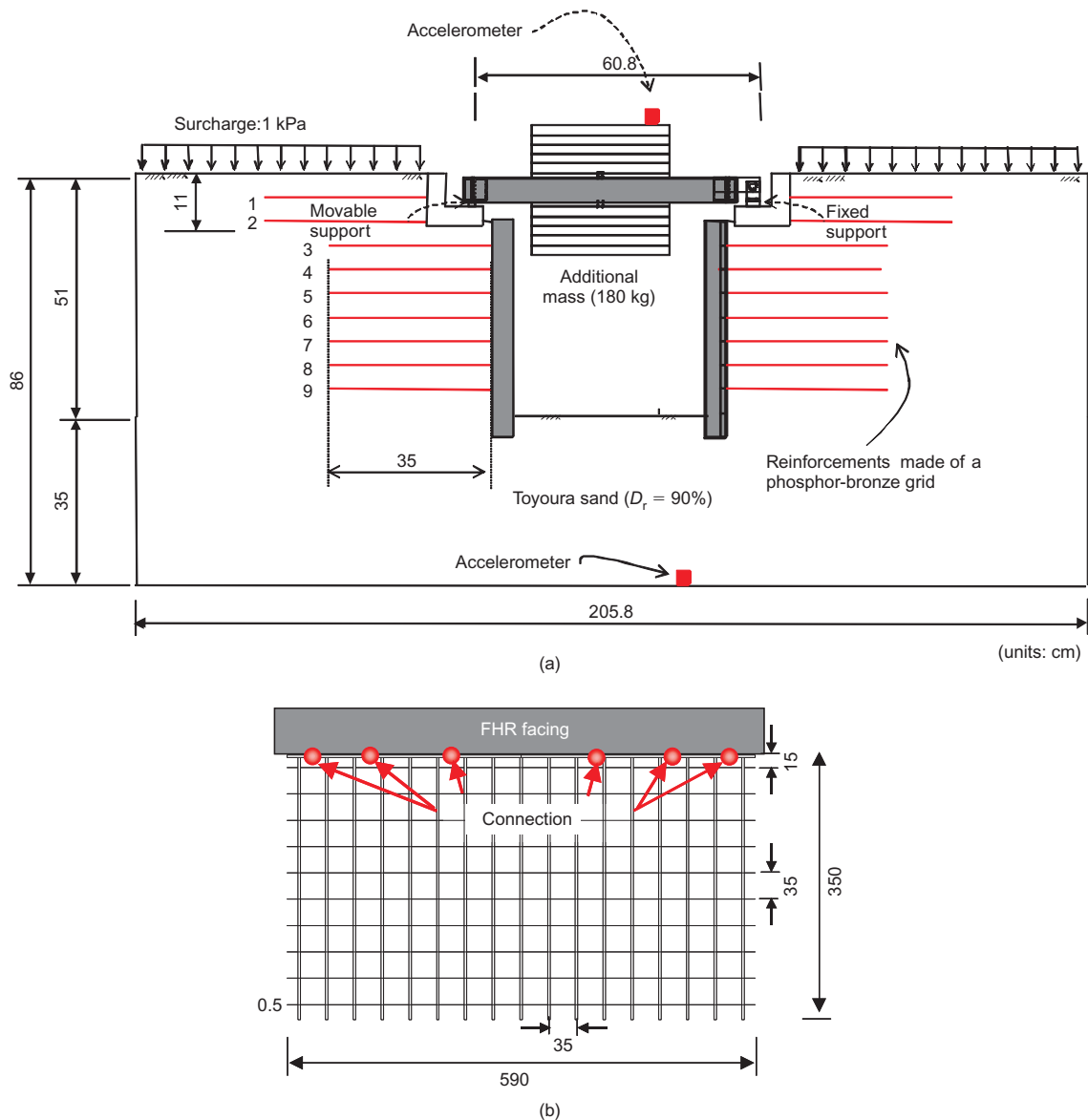
Figure 3. (a) GRS-RW bridge model; (b) phosphor-bronze grid connected to facing (Tatsuoka *et al.* 2009)

sand, dyed black, were placed at a vertical spacing of 10 cm immediately behind the front transparent glass window of the sand box (as shown in Figure 11, for example). The models were densely instrumented at locations relevant to monitor displacements, earth pressures and accelerations (and tensile forces in the model reinforcement layers in the backfill, when used).

2.2.2. Geosynthetic-reinforced soil-retaining wall bridge (GRS-RW bridge; Figure 3)

This bridge model comprises a girder supported via bearings by a pair of GRS-RWs having a stage-constructed FHR facing. In Figure 3a, the left end of the girder is supported by a movable bearing, and the right end is by a fixed bearing. The bottom of the facing was embedded 4 cm in the subsoil of air-dried Toyoura sand. In total, seven layers of reinforcement were arranged at a vertical spacing of 5 cm in the backfill, and connected to the facing on each side by using six bolts for a width of 59 cm per layer (Figure 3b).

Geogrid layers used in actual field cases were simulated by a set of regular grids comprising longitudinal members (made of thin and narrow phosphor-bronze strips, 0.2 mm thick and 3 mm wide, with a rupture strength of 359 N per strip), welded at nodes to transverse members (made of mild steel bar, 0.5 mm in diameter). The surface of the strips was made rough by gluing particles of Toyoura sand (Aizawa *et al.* 2008). Two reinforcement layers at a vertical spacing of about 5 cm were connected to the back face of the respective sill beams placed on the crest of the respective GRS-RWs in the same way as the reinforcement layers connected to the FHR facings.

2.2.3. Integral bridge (IB; Figure 4)

The girder and the FHR facings were structurally connected to each other with a pair of L-shaped metal fixtures (20 cm long, 5 cm wide and 3 mm thick). The peak resisting moment obtained from the relationship between the moment, M, and the flexural angle, ϕ, obtained by a bending test (Figure 4b) is equal to about 0.5 kN m. This
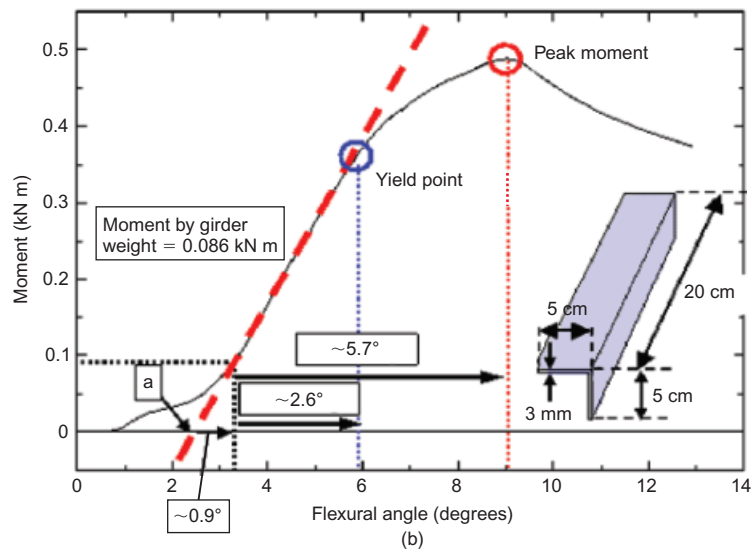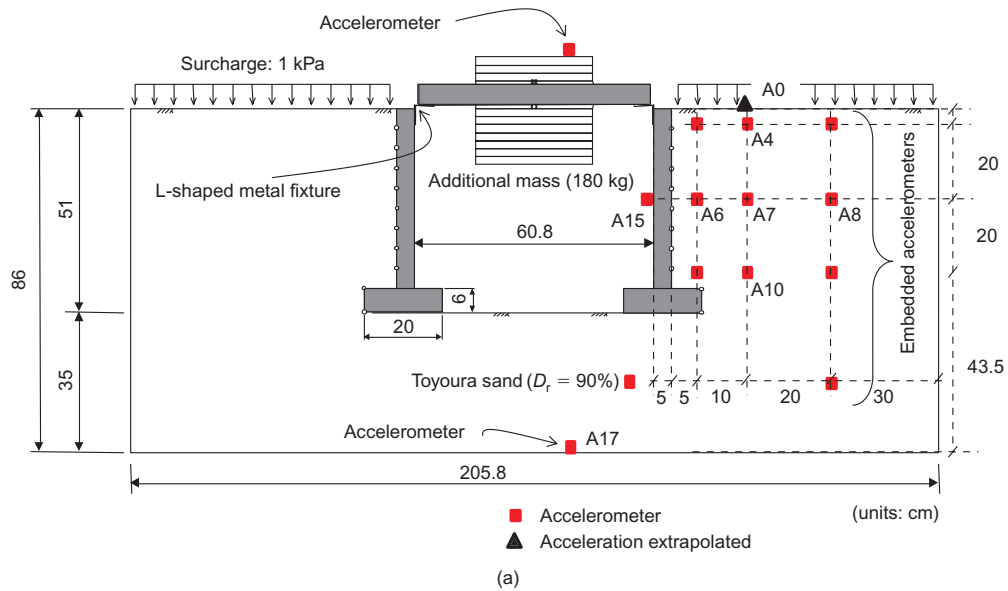
Figure 4. (a) Integral bridge model (all accelerometers indicated); (b) bending properties of L-shaped metal connector (i.e. fixture) (Tatsuoka *et al.* 2009).
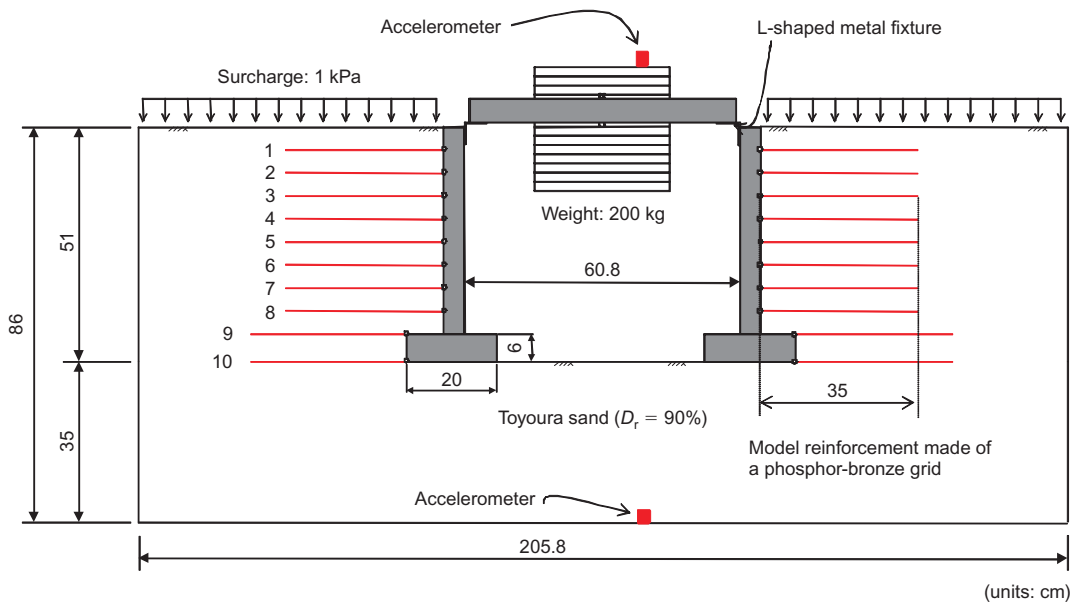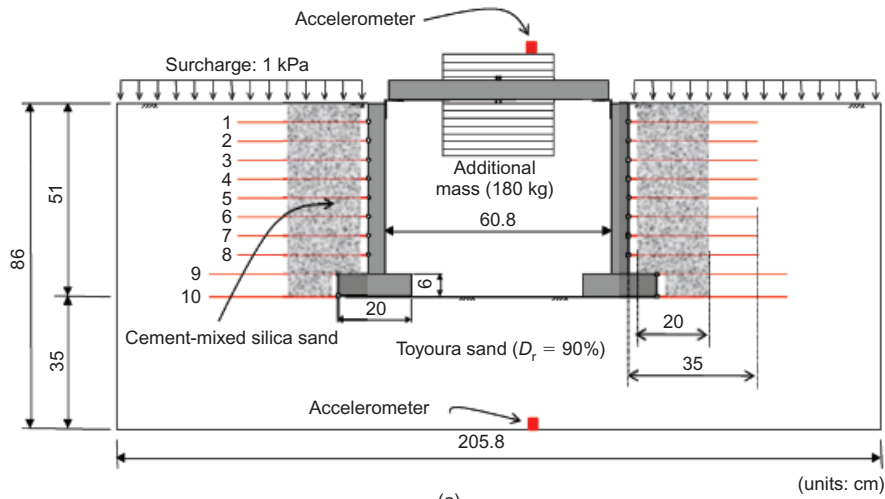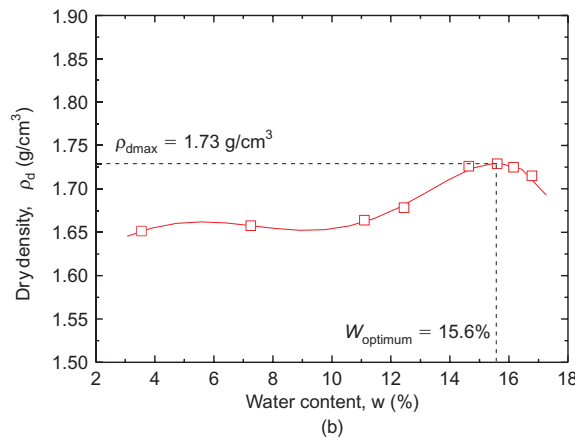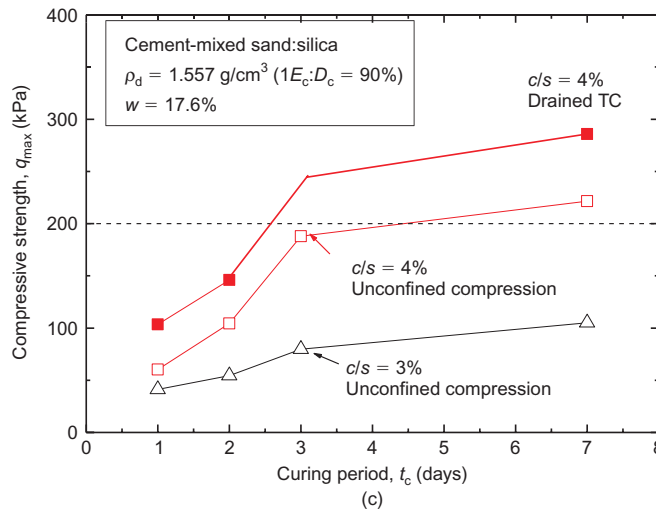

Figure 5. GRS integral bridge model (Tatsuoka *et al.* 2009)

Figure 6. (a) GRS integral bridge with rectangular prismatic cement-mixed soil zone; (b) compaction curve; (c) strength against curing time for cement-mixed silica sand No. 6 (Nishikiori 2007)

strength is much smaller, by a factor of about 1/3, than the moment produced by the earth pressure activated on the back of the facing when this bridge model starts failing (Tatsuoka *et al.* 2009). That is, the fixtures were designed not to become the major resisting structural component when failure of the bridge was imminent. This arrangement was adopted to simulate the dynamic behaviour of a full-scale bridge after the fixture, which is the weakest structural part, has yielded flexurally during dynamic loading. A study of the effects of the strength of the fixture on the dynamic stability of bridge system will be necessary in the future.

2.2.4. *Geosynthetic-reinforced soil integral bridge (GRS-IB; Figure 5)*
The girder and a pair of FHR facings were integrated to each other in the same way as in the IB model. In total, 10 reinforcement layers were arranged in the backfill on each
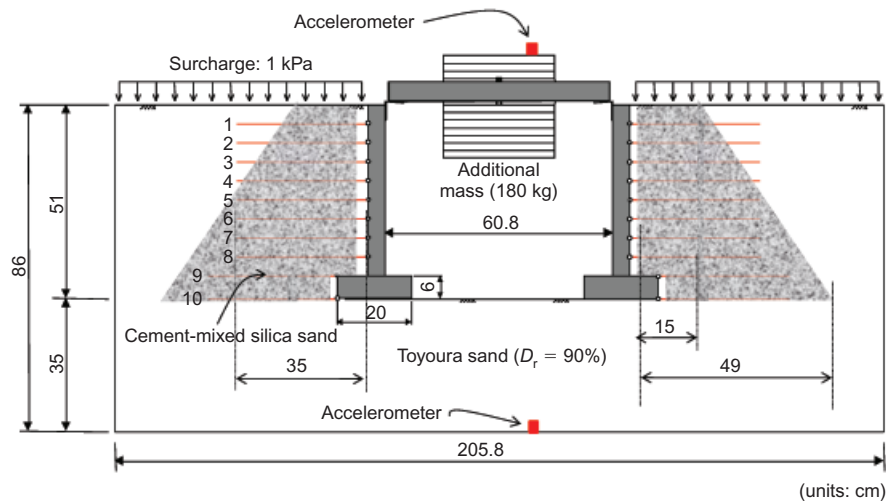
Figure 7. GRS integral bridge model with trapezoidal zone of cement-mixed soil (adapted from Soma *et al.* 2009)

side: eight layers were connected to the back of the facing at a vertical spacing of 5 cm, and two layers to the back of the facing foundation at a vertical spacing of 6 cm. Each layer was connected to the FHR facing and foundation by using six bolts for a width of 59 cm per layer (Figure 3b) so that high connection strength was ensured to make the pullout failure take place eventually (Hirakawa et al. 2007).

2.2.5. GRS integral bridge with rectangular prismatic cement-mixed sand zone (GRS-IB-C, Figure 6)

This bridge model is the same as the GRS-IB model described above, except that a rectangular prismatic zone of cement-mixed silica sand (20 cm long, 60 cm wide and 51 cm high), made as follows, was arranged immediately behind the facing.

(a) Silica sand No. 6 ($e_{max} = 1.174$, $e_{min} = 0.671$, $G_s = 2.65$, $U_c = 1.64$, $D_{50} = 0.29$ mm) was mixed with ordinary Portland cement at a mixing ratio by weight, c/s, equal to 4.0%.

(b) The sand–cement mixture was mixed with tapwater at a water content of 17.6%, which is larger by 2% than the optimum water content by the standard Proctor test (i.e. $1E_c$ by the JIS A 1210 (2009), A-b method; Figure 6b).

(c) The mixture was compacted to a dry density $\rho_d = 1.557$ g/cm^3 (i.e. a degree of compaction equal to 90%). By postulating that the unconfined compression strength, q_u, required for full-scale structures is equal to 2 MPa, and based on a scale factor for stress of $1/\lambda = 1/10$, a target value of q_u, $(q_u)_{model} = 200$ kPa at the curing time when the shaking table test was to be performed, equal to 4 days, was determined. Then the mixing proportion and compaction conditions to obtain this $(q_u)_{model}$ value were determined, based on the results of unconfined compression tests (Figure 6c). In this figure, for reference, the compression strength from drained triaxial compression tests at a confining pressure of 10 kPa is also presented.

(d) The cement-mixed sand zone (Figure 6a) was

produced by manual tamping using a wooden hammer in a compacted lift of 5 cm, equal to the vertical spacing between vertically adjacent model reinforcement layers. A thin (3 cm wide) vertical layer of uncemented silica sand was arranged between the facing and the cement-mixed sand to simulate the buffer zone to absorb relative displacements used in prototype structures.

2.2.6. GRS integral bridge with trapezoidal cement-mixed sand zone (GRS-IB-C-T; Figure 7)

This bridge model is the same as GRS-IB-C, described above, except that the shape of the cement-mixed silica sand zone is trapezoidal, with a base length of 49 cm; a top length of 15 cm; a height of 51 cm; and a width of 60 cm. A cement-mixed gravelly soil zone of this shape is often constructed immediately behind full-scale bridge abutments for high-speed railways in Japan (Tatsuoka *et al.* 2005, 2009). Two models of GRS-IB-C-T were constructed. The first one was subjected to sinusoidal base acceleration motion at a frequency, f_i, equal to 5 Hz, as the other bridge models and the second, named GRS-IB-C-T-*f*, was subjected to base acceleration with a wide range of frequency.

2.3. Dynamic loading method

Except for the test of GRS-IB-C-T-*f*, each bridge model was subjected to sinusoidal base acceleration motion at $f_i = 5$ Hz with 20 cycles per stage. The acceleration amplitude was increased stage by stage with a target increment of 100 gal (1 gal = 0.01 m/s^2) from 100 gal to until failure and then collapse took place (Figure 8a). $f_i = 5$ Hz was selected to be lower than the initial natural frequency of the models (listed in Table 1) by considering that the typical predominant frequencies of strong earthquake motions at full scale (1–3 Hz) are lower than the natural frequencies under undamaged conditions of ordinary full-scale bridges, including GRS integral bridges that are larger by a scaling factor of 10 than the bridge models tested in this study. Only the GRS-IB-C-T model was also subjected to sinusoidal base acceleration histories of multiple frequencies, $f_i = 2$–3, 5, 10, 15, 20, 25 and
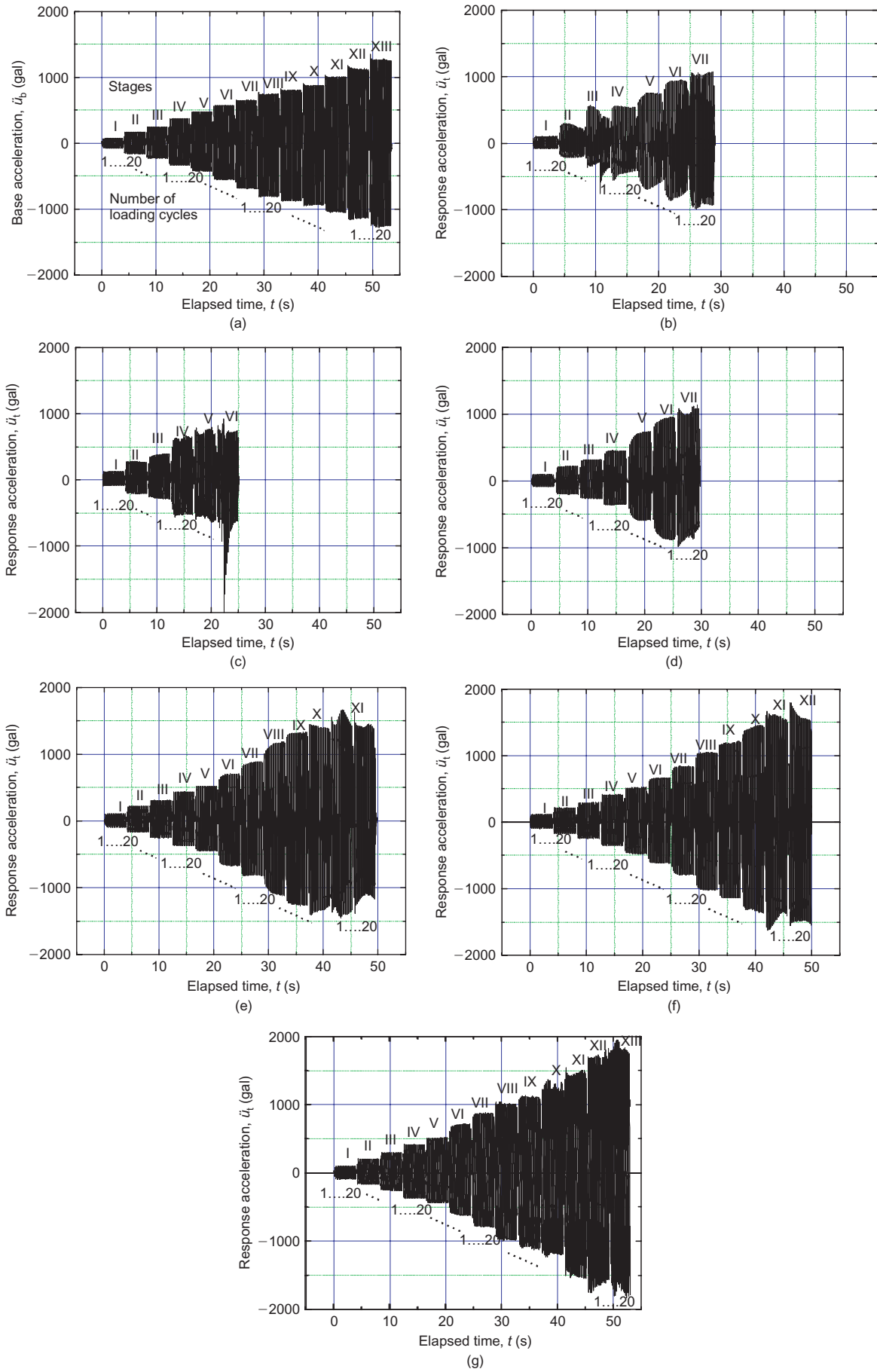
Figure 8. Time histories of (a) representative base acceleration (used in test on GRS-IB-C-T), and response acceleration at girder of: (b) conventional bridge; (c) GRS-RW bridge; (d) integral bridge; (e) GRS-IB; (f) GRS-IB-C; (g) GRS-IB-C-T (Roman numerals I, II, II etc. denote loading stages)

30 Hz at different stages to evaluate the effects of f_i on the dynamic response of the structure.

3. DYNAMIC RESPONSE AS AN SDOF SYSTEM

3.1. Modelling the bridge models as an SDOF system

Figure 9 summarises the load and resistance components for the rotation of the FHR facing relative to the backfill, which is the most critical dynamic failure mode for GRS integral bridges observed in the shaking-table tests (Tatsuoka *et al.* 2009). The two major resisting components are the passive pressure in the upper part of the backfill, and the tensile force of the reinforcement at the lower part of the facing. In the present study, it was examined whether the former can be increased by arranging a lightly cement-mixed sand zone immediately behind the facings (i.e. GRS-IB-C and GRS-IB-C-T, Figures 6 and 7). The displacement and deformation mode illustrated in Figure 9 is the first mode of the dynamic behaviour of the integral bridge models (i.e. IB, GRS-IB, GRS-IB-C and GRS-IB-C-T). The first mode is dominant over the other modes because these integral bridge models are top-heavy structures, while the flexural rigidity of the facing is very high compared with the relatively low coefficients of the subgrade reaction of the surrounding backfill and subsoil. The six bridge models (Table 1) were modelled as damped, single-degree-of-freedom (SDOF) systems, and their dynamic behaviour was analysed following the method developed by Shinoda *et al.* (2003). The dynamic behaviour mode of the bridge models using bearings to support a girder (i.e. CB and GRS-RW; Figures 2 and 3) deviates from that illustrated in Figure 9: therefore, modelling as an SDOF system is more approximate, particularly when the failure is imminent.

3.2. Equations of motion for an SDOF system

The equation of motion for an SDOF system subjected to dynamic base shaking $\ddot{u}_b$ is

Figure 9. Load and resistance components for facing rotation, GRS integral bridge (Tatsuoka *et al.* 2009)

$$m\ddot{u}_t(t) + c\dot{u}(t) + ku(t) = 0 \quad (1)$$

where $\ddot{u}_t$, the total acceleration of the equivalent mass at the top of the system, is the sum of $\ddot{u}_b$ and the relative acceleration to the base, $\ddot{u}$,

$$\ddot{u}_t = \ddot{u}_b + \ddot{u} \quad (2)$$

and m, k and c are the mass, stiffness and damping, respectively, of the system, and t is a particular time. It was assumed that the bridge models were subjected to exactly uniform sinusoidal base shaking, $\ddot{u}_b$,

$$\ddot{u}_b = -\text{Amp}[\ddot{u}_b] \cdot \sin \omega_i t \quad (3)$$

where $\text{Amp}[\ddot{u}_b]$ is the amplitude of $\ddot{u}_b$. The total response comprises: the transient response, which is controlled by the initial conditions, and decays with time; and the steady-state response, which describes the displacement after the transient response has died out. In the present study, the damping ratio of the bridge models was very high (as shown later), and the transient response died out very quickly. Hence, except for the first cycle of the shaking stage, the total response could be described fairly accurately by the steady-state response as

$$\ddot{u}_t - \text{Amp}[\ddot{u}_b] \cdot M \sin(\omega_i t + \phi) \quad (4)$$

where M is the magnification ratio of the response acceleration, defined as the ratio of the amplitude of the total acceleration, $\text{Amp}[\ddot{u}_t]$, to the amplitude of the base acceleration, $\text{Amp}[\ddot{u}_b]$; and ϕ is the phase difference. The values of M and ϕ are obtained as

$$M = \sqrt{\frac{1 + 4\xi^2\beta^2}{(1 - \beta^2)^2 + 4\xi^2\beta^2}} \quad (5)$$

$$\phi = \arctan\left[\frac{-2\xi\beta^3}{1 - (1 - 4\xi^2)\beta^2}\right] \quad (6)$$

where $\omega_0 = \sqrt{k/m}$ is the natural circular frequency of the system, equal to $2\pi f_0$, where f_0 is the natural frequency; ω_i is the input circular frequency, equal to $2\pi f_i$; ξ is the damping ratio, equal to $c\omega_0/2k$; and β is the tuning ratio, equal to $\omega_i/\omega_0 = f_i/f_0$.

In the analysis of the shaking table test data, the values of M and ϕ were obtained directly from the time histories of accelerations at the shaking table and the girder (Figure 8), which were fitted by sinusoidal time histories. With known values of M and ϕ at respective moments, the values of β and ξ were back-calculated by iteration (i.e. by Newton's method), based on Equations 5 and 6. The values of β and ξ, which represent the transient stiffness condition and energy dissipation capacity of the various bridge models, are the two essential parameters that control the dynamic behaviour in the present study. During the various dynamic loading histories, an increase in β was associated with a decrease in the stiffness due to damage to the structure by dynamic loading.
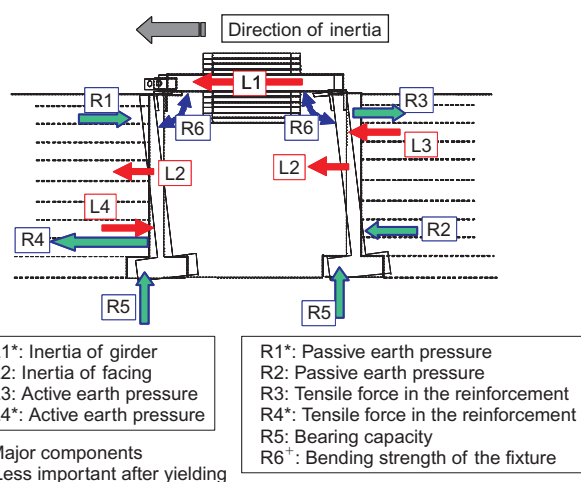
4. CRITERIA TO EVALUATE DYNAMIC STABILITY

4.1. General

The dynamic stability of a bridge is basically controlled by:

1. the strength to resist the response acceleration;
2. the initial stiffness;
3. the softening rate, which controls the process of approaching the resonance state; and
4. the damping capacity, which controls the response acceleration for a given input acceleration at failure.

In static loading cases, the strength (property 1) and the stiffness (part of properties 2 and 3) are of major concern. Table 1 summarises the initial natural frequency and the part of these features evaluated at failure of the bridge models.

4.2. Strength

With full-scale civil engineering structures, failure is usually associated with deformations or displacements, such as settlement, bumps, displacement, rotation, or cracking in steel-reinforced concrete structures, that exceed specified serviceability limit values. In the present study, the strength of a given bridge model is defined as the amplitude of the response acceleration at the girder when the model starts to exhibiting significant deformation and displacements, $\text{Amp}[\ddot{u}_t]$. In all the model tests using sinusoidal base acceleration at $f_i = 5$ Hz, failure did not occur before the transient resonance state was reached, where $\beta = \beta_{\text{resonance}}$, and the maximum value of M, M_{peak}, was observed. In these tests, at the resonance state, a large response took place, inducing large deformation and displacement. The resonance was followed by a rapid process towards the collapse state, owing to a rapid decrease in M from M_{peak} associated with a fast increase in β from $\beta_{\text{resonance}}$. That is, none of the bridge models could not survive the resonance state. Therefore the strength of a given bridge model, which represents the largest dynamic load that the system can withstand without exhibiting severe damage, is defined by the response acceleration amplitude at the transient resonance, $\text{Amp}[\ddot{u}_t]_{\text{resonance}}$ (Table 1).

The amplitude of each of the 20 single-base sinusoidal waves, $\ddot{u}_b$, varied slightly for the various loading stages (denoted I, II, III, etc. in Figure 8). This was probably due to changes in the compliance of the shaking table with the model. However, as seen from Table 1, the maximum table acceleration at resonance, $\text{Amp}[\ddot{u}_b]_{\text{resonance}}$, and the maximum table acceleration, $\text{Max}[\ddot{u}_b]$, during the stage when resonance occurred are nearly the same in all the tests.

4.3. Initial stiffness

As the initial (i.e. undamaged) stiffness of a given bridge becomes larger – that is, as the initial value of the natural frequency, f_0, becomes larger – the initial value of the tuning ratio, $\beta = f_i/f_0$, becomes smaller. Then the initial response becomes smaller, reducing the possibility of failure.

4.4. Softening rate

As the softening rate of a given bridge, defined as the increasing rate of β with an increase in the number of loading cycles or the input acceleration level, becomes smaller (i.e. as the bridge becomes more dynamically ductile), β increases at a slower rate for a given time history of input acceleration. he bridge does not then rapidly approach the resonance state, where $M = M_{\text{peak}}$ and $\beta = \beta_{\text{resonance}}$. The response is kept small, and the possibility of failure is kept low. When the bridge approaches and then reaches its resonance state when subjected to strong base acceleration, it becomes dynamically less ductile by being more damaged, and softer. The rate at which β approaches $\beta_{\text{resonance}}$ (~ 1.0) is increased, resulting in an increased possibility that failure will occur at the resonance state. The process towards ultimate collapse, in which β continues to increase from unity, may then follow.

4.5. Damping capacity

The maximum response acceleration at the girder anticipated for a given design earthquake motion is one of the crucial seismic design factors. The upper bound of this value is equal to the product of the magnification ratio M at the resonance state (i.e. M_{peak} at $\beta = \beta_{\text{resonance}}$) and a given design peak horizontal ground acceleration, PGA. The magnification ratio, M, decreases with an increase in the capacity of the structure to dissipate energy, represented by the damping ratio, ξ. The damping ratio consists of: the material damping, which is controlled mainly by the maximum shear strain attainable in the backfill as part of the bridge system; and the dissipation damping by wave propagation radiating from the bridge system towards the backfill and supporting ground outside the considered bridge system.

The dynamic behaviour of the various bridge models are evaluated below, based on the above four criteria.

5. FAILURE PATTERNS OF THE BRIDGE SYSTEMS

5.1. Overall behaviour of the six models

Figure 10a summarises the relationships between the response acceleration at the girder and the input acceleration at the shaking table of the six models when the input acceleration increases stage by stage at $f_i = 5$ Hz. Figure 10b shows the relationships between the response acceleration at the girder and the tuning ratio, $\beta = f_i/f_0$, back-calculated based on Equations 5 and 6. In Figure 10b and the other figures, results from the SDOF analysis at the first cycle of several stages in which the response is obviously transient are not plotted. The following trends may be seen from Figures 10a and 10b:

1. With each model, the response acceleration is similar to the input acceleration at the initial stage, and it
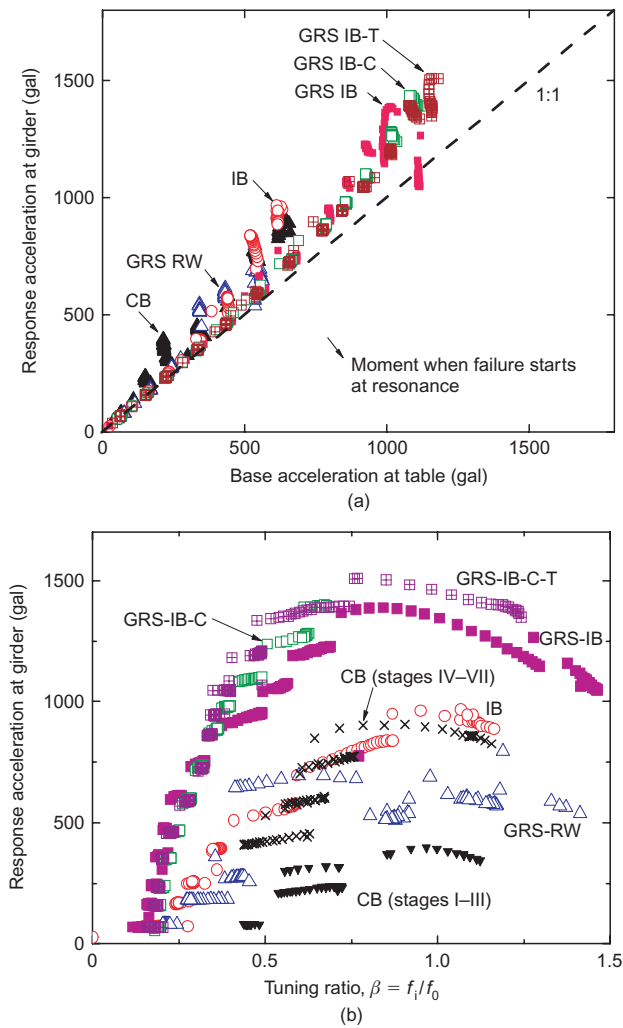
Figure 10. For all models: (a) response acceleration at girder against input acceleration at table; (b) response acceleration at girder against tuning ratio ($f_i = 5$ Hz)

becomes larger than the input acceleration as the input acceleration increases.

2. The largest response acceleration at the girder takes place when the tuning ratio β approaches unity and the resonance state is reached. Subsequently, the response acceleration decreases, despite an increase in the input acceleration.

3. The rate of the increase in β with an increase in the response acceleration at the girder decreases with an increase in the amplitude of the response acceleration at resonance, Amp$[\ddot{u}_t]_{resonance}$ (i.e. an increase in the strength). Consequently, as the strength increases, the resonance state is reached later (i.e. at a larger amplitude of input acceleration).

These trends are analysed in detail below.

5.2. Conventional bridge (CB)

This bridge model failed when the response acceleration at the girder, Amp$[\ddot{u}_t]_{resonance}$, became 397 gal at stage III. Immediately after the start of stage I, M was 1.25 and β was 0.48 (Figure 11a). In this figure, and similar ones in

this paper, the continuous lines are the theoretical curves for different damping ratios obtained from Equations 5 and 6, and data points represent the measured values of M and ϕ plotted against the respective values of β. At stage II and then stage III, M increased considerably, associated with a large increase in β with cyclic loading, until it became M_{peak} ($= 1.85$) and β became $\beta_{resonance}$ ($= 0.97$) at state III(5). Subsequently, the transient resonance state was passed, and β became larger than unity. Figure 11b shows the phase difference ϕ for each loading cycle at each stage. The value of ϕ increased from a value close to zero, associated with an increase in β.

The values of β and ϕ increased very rapidly, particularly at stage III, where failure started to occur. That is, as seen from Figure 11c, the abutment supporting the girder via a fixed (i.e. hinged) bearing started to rotate significantly, about the toe of its base, with a large active movement of the top separating from the backfill. This trend resulted in the development of significant shear bands (active failure planes) in the backfill. Correspondingly, the crest of the backfill within a range of more than 20 cm from the back face of the abutment settled significantly. This type of failure has occurred in many full-scale conventional bridges during major earthquakes.

With the CB model, an increase in the value of β is due to a decrease in the stiffness, k, of the bridge system caused by a decrease in: (1) the coefficients of subgrade reaction at the interface between the abutments and the backfill and supporting ground; and (b) the stiffness of the backfill and supporting ground (particularly after shear bands start to develop in the backfill associated with large outward lateral displacements of the abutments). With the integral bridge models (described below), the stiffness, k, also decreases with a decrease in the stiffness of the fixtures between the girder and the facings. A decrease in k may result in progressive failure, and ultimately in collapse. That is, a decrease in the stiffness of a given bridge system by degradation of any component accelerates the process of approaching the resonance state, which then results in further degradation of the components, which then accelerates the process of the bridge system approaching failure, and ultimately collapse. This process was common with all the bridge models examined in the present study, whereas the rate of approach towards the resonance state was very different among these models.

In the test on the CB model, at stage III the left end of the girder made contact with the top of the abutment, owing to large displacements at the movable bearing. The stiffness of the bridge model was then recovered, and β became much smaller than 0.5, resulting in a decrease in M to 1.2, at the start of stage IV (Figure 11a). Subsequently, the values of M and β started to increase again, associated with a continuous decrease in the stiffness of the bridge, until β became $\beta_{resonance} = 0.91$ and M became $M_{peak} = 1.43$ at stage VII (Amp$[\ddot{u}_t]_{resonance} = 906$ gal). The second Amp$[\ddot{u}_t]_{resonance}$ value is much larger than the first at stage III (Figure 10b). However, the second M_{peak} value is significantly smaller than the first. This is due to a significant increase in the damping ratio ξ, caused both by
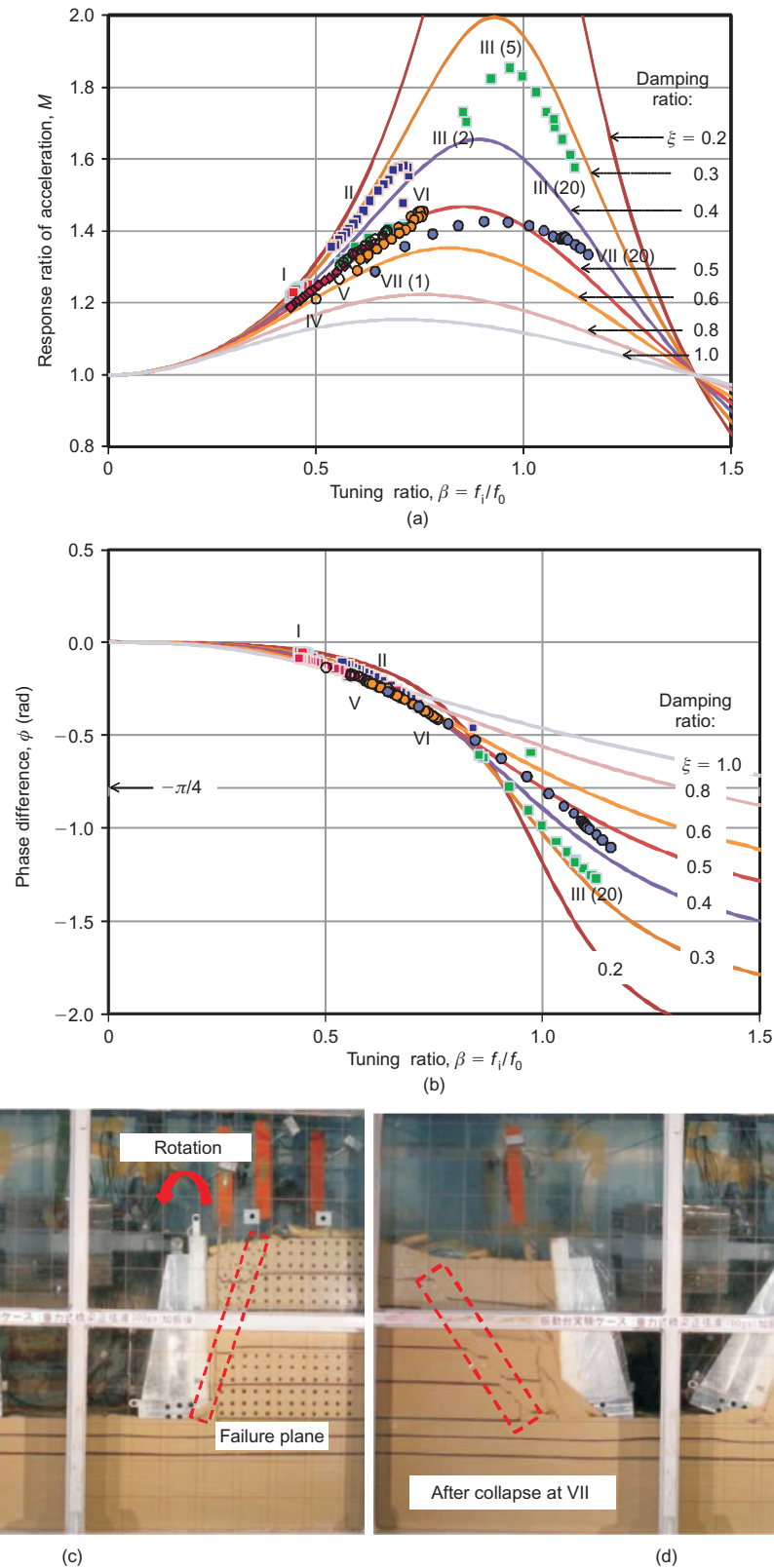
Figure 11. Performance of CB model for $f_i = 5$ Hz at all stages: (a) M against β; (b) ϕ against β; (c) deformations observed after failure; (d) deformations observed after collapse

severe damage to the system and by an increase in the degree of structural integration caused by contact of the free end of the girder to the abutment. At stage VII, the bridge model finally collapsed: that is, the abutments rotated significantly, and their bases were largely pushed out, with the development of significant shear bands in the backfill and a substantial decrease in the coefficient of subgrade reaction (Figure 11d).

The dynamic stability of the CB model is the lowest among all the tested bridge models. This is due to the poor performance of the two weakest components of the bridge system: the bearings and the unreinforced backfill.

In particular, progressive dislodging of the girder at the movable bearing makes the seismic stability of this bridge type very low.

5.3. Geosynthetic-reinforced-soil-retaining wall bridge (GRS-RW bridge)

This model failed when $\text{Amp}[\ddot{u}_t]_{\text{resonance}} = 546$ gal at stage IV. At the beginning of stage I, the values of M and β were small, equal to 1.06 and 0.21 (Figure 12a). Both M and β increased gradually in stages II and III, and then very fast in stage IV, when eventually M became $M_{\text{peak}} = 1.60$ when β became $\beta_{\text{resonance}} = 0.85$ and failure occurred. Subsequently, the resonance state was passed, and the value of β became larger than unity. The value of ϕ increased from close to zero, and became large at stage IV, where failure occurred (Figure 12b). That is, as seen from Figure 12c, the sill beam supporting the girder via a fixed bearing exhibited noticeable settlement and rotation about a point near the toe, which induced a noticeable rotation and settlement of the girder and settlements in the backfill immediately behind the sill beam. By contrast, the GRS-RWs with an FHR facing performed very well without exhibiting any noticeable tilting, lateral displacement or settlement of the facing, and without any noticeable shear bands in the reinforced backfill. With cyclic loading at stage IV and then with an increase in the input acceleration level by proceeding from stage IV to stage V, the rotation of the sill beam became more significant, producing larger settlements in the backfill crest. Eventually, noticeable shear bands developed in the reinforced backfill behind the sill beam. A rapid increase in the value of β value was primarily due to a low bearing capacity of the backfill underneath the sill beam against severe eccentric load, although the backfill was reinforced. It seems that the top reinforcement layer (5 cm deep from the base of the sill beam) did not increase the bearing capacity sufficiently. Moreover, the development of shear bands in the reinforced backfill behind the sill beam reduced the stiffness of this backfill portion, resulting in an overall decrease in the stiffness of the bridge system.

At stage VI ($\text{Amp}[\ddot{u}_t]_{\text{resonance}} = 689$ gal), the free end (i.e. the left end) of the girder made contact with the sill beam, owing to large displacements at the movable bearing (Figure 12d). Then the stiffness of the system was recovered, and the value of β decreased from 1.41 (state VI(1)) to 0.41 (state VI(20)) (Figure 12a). In this process, the second peak, $M_{\text{peak}} = 1.31$, occurred. By the end of this stage, the system finally collapsed: that is, the sill beam rotated significantly, which resulted in a large, uneven displacement of the girder.

In summary, the GRS-RW bridge model performed much better than the CB model. As can be seen from Table 1, the CB model reached failure when the base acceleration was as low as 214 gal, whereas the GRS-RW bridge model reached failure at 341 gal. Yet the strength of the GRS-RW bridge model was not very high, owing to the low stability of the sill beam supporting the girder via a fixed bearing, whereas the GRS-RWs were very stable. Therefore a new bridge type that has the bearings removed, called the GRS integral bridge, was developed.

5.4. Integral bridge (IB)

This bridge model failed when $\text{Amp}[\ddot{u}_t]_{\text{resonance}} = 838$ gal at stage VI, showing that it is much more stable than CB model, which failed at 397 gal, and more stable than the GRS-RW bridge model, which failed at 546 gal (Table 1). With the IB model, the initial values of M and β values were lower (i.e. $M = 1.07$ and $\beta = 0.27$). At stage VI, both M and β increased very rapidly with cyclic loading until M became M_{peak} ($= 1.61$) when β became $\beta_{\text{resonance}}$ ($= 0.87$) at state VI(20) (Figure 13a). After having passed the transient resonance state, the β value continued to increase. Figure 13b shows how the value of ϕ increased during this test. The increase in the values of β and ϕ was associated with a decrease in the stiffness of the bridge system caused by degradation of the following three resisting components:

1. the coefficient of subgrade reaction at the interface between the facings and the backfill and supporting ground;
2. the stiffness of the backfill and supporting ground, particularly after shear bands developed, associated with large outward lateral displacements of the facings; and
3. the stiffness of the L-shaped fixtures.

After all these resisting components had largely deteriorated, the whole system collapsed at stage VII (the maximum acceleration at the girder, $\text{Max}[\ddot{u}_t] = 945$ gal), at which the facings rotated significantly, with large push-out at the bottom. The crest of the backfill settled down significantly, associated with significant development of shear bands in the backfill, which was recorded not only 5 cm but also 35 cm back from the facing (Figure 13d).

5.5. GRS integral bridge (GRS-IB)

This model failed at state XI(7), where $\text{Amp}[\ddot{u}_t]_{\text{resonance}} = 1{,}374$ gal and $\beta = \beta_{\text{resonance}} = 0.92$ (Figure 15a). This result shows a considerably higher dynamic stability, higher than that not only of the CB model but also of the GRS-RW model and IB model (Table 1). Figure 14b shows how the value of ϕ increased. By comparing Figures 13a and 14a, it may be seen that the GRS-IB model became much stronger than the IB model by reinforcing the backfill with reinforcement layers connected to the facings. That is, at the end of stage VI (i.e. at state VI(20)), the GRS-IB model exhibited $M = 1.07$ when $\beta = 0.26$, whereas the IB model exhibited a much higher value of M at resonance, $M_{\text{peak}} = 1.61$, at a much larger β, $\beta_{\text{resonance}} = 0.87$ (Figure 13a). The GRS-IB model reached its resonance state at state XI(7), at which M_{peak} was 1.38 at $\beta = \beta_{\text{resonance}} = 0.92$ (Figure 14a). The fact that this M_{peak} value is noticeably lower than the M_{peak} value at resonance of the IB model ($= 1.61$) indicates a higher damping capacity of the GRS-IB model than that of the IB model. This trend is due to the following two factors. By reinforcing the backfill, the shear strain in the backfill that could become at failure increased, therefore, the material damping of the backfill
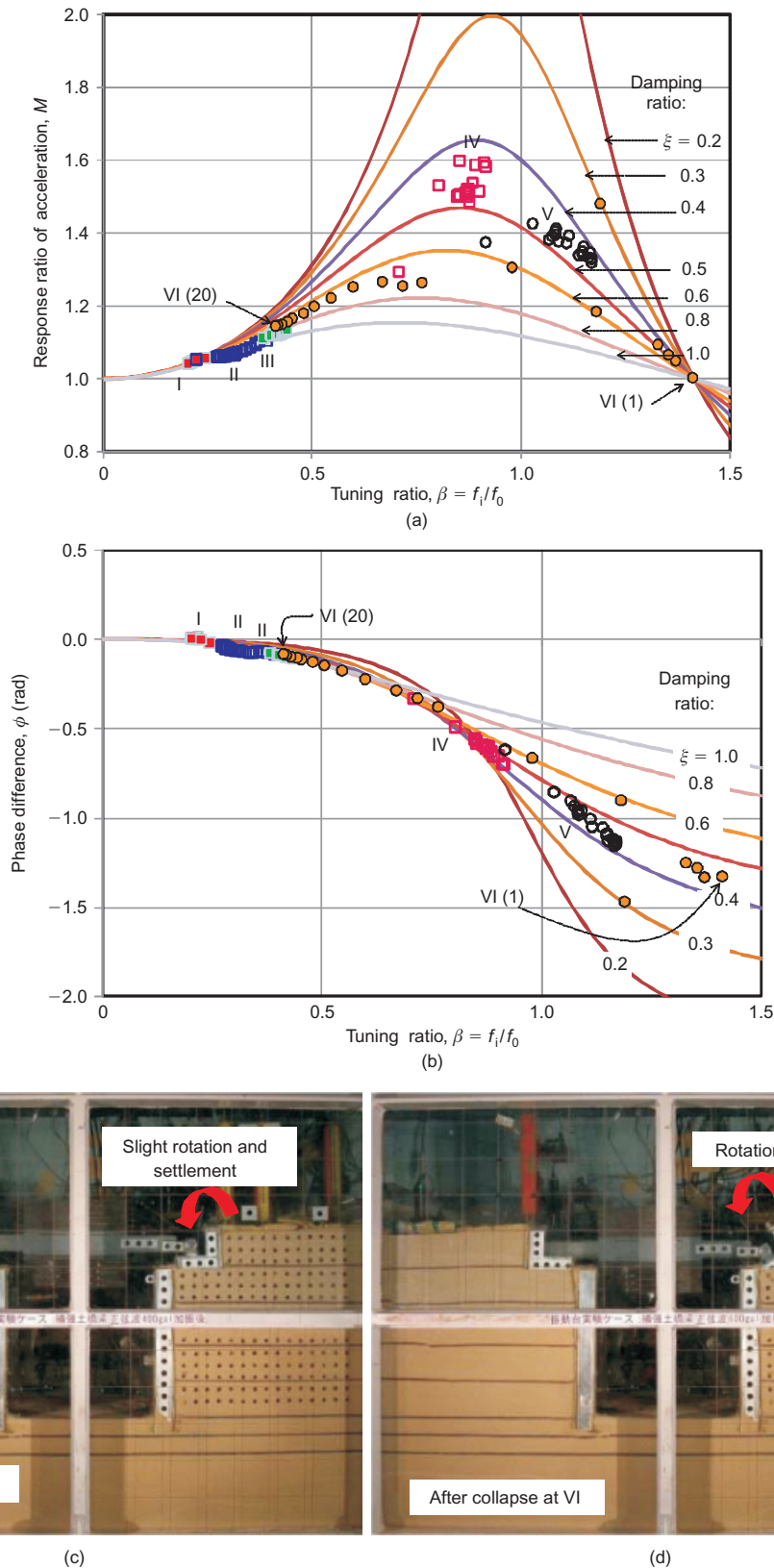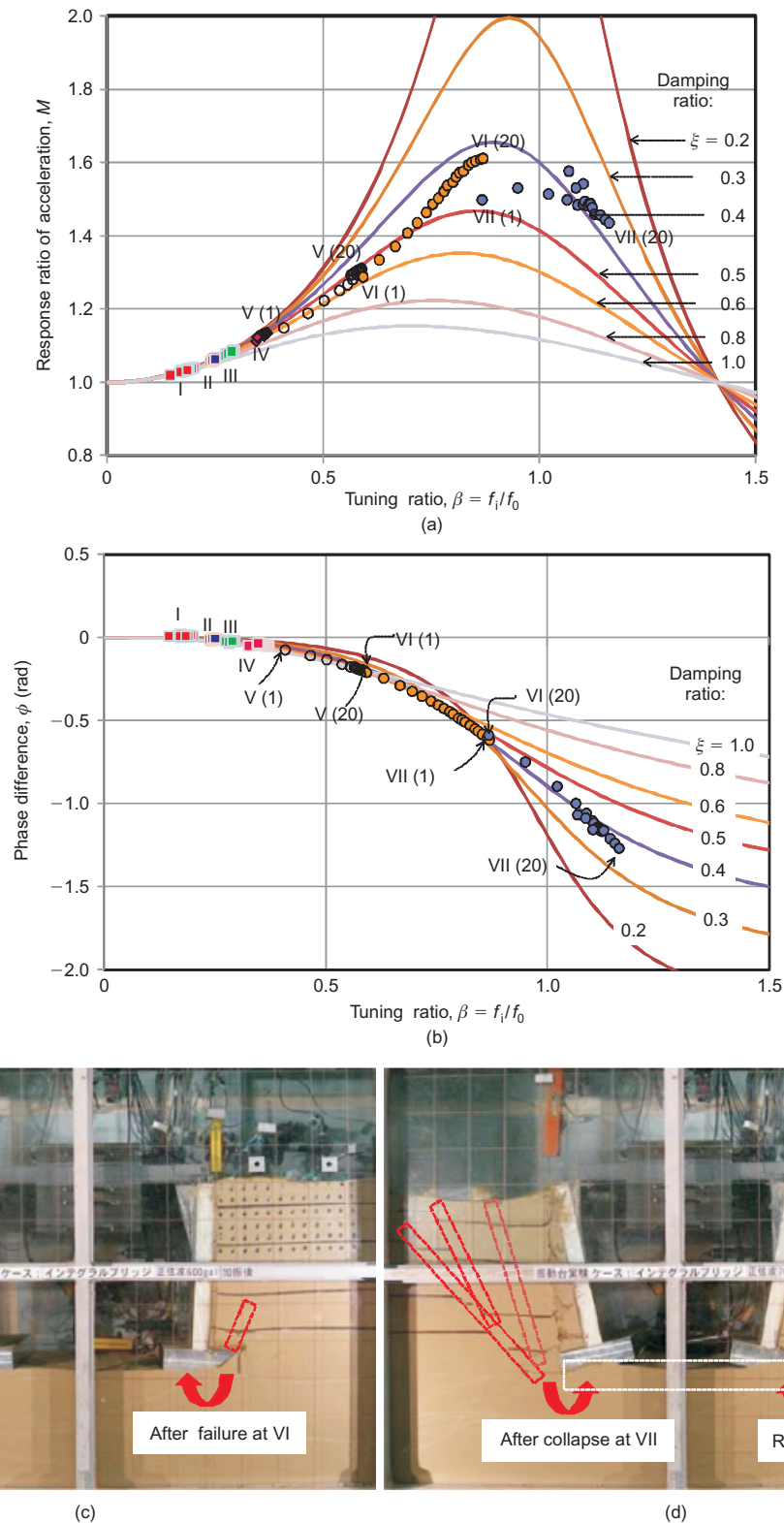
Figure 12. **Performance of GRS-RW bridge for $f_i = 5$ Hz at all stages: (a) M against β; (b) ϕ against β; (c) deformations observed after failure; (d) deformations observed after collapse**

became larger; and more dynamic energy could be dissipated from the bridge system to a larger mass of backfill and supporting ground. The observed damping ratio ξ as an SDOF of the GRS-IB model at resonance is about 55%, which is too high as the material damping of

the backfill. This is probably because this ξ value includes dissipation damping by wave propagation, as discussed in detail later.

The GRS-IB model also has a higher initial stiffness and a larger dynamic ductility than the IB model. That is,

Figure 13. Performance of IB for $f_i = 5$ Hz at all stages: (a) M against β; (b) ϕ against β; (c) deformations observed after failure; (d) deformations observed after collapse

at stage X (Max[$\ddot{u}_t$] = 1227 gal), the backfill immediately behind the facings started heaving slightly, caused by passive movements at the top of the facing. Subsequently, as the rotation of the facings progressively increased, shear bands gradually developed in the unreinforced backfill zone immediately behind the reinforced zones. Neverthe-

less, the reinforced backfill zone was still very stable, exhibiting rather monolithic behaviour, without distinct shear bands formed inside. In this way, a significant decrease in the stiffness of the bridge model was delayed, keeping the value of β much lower than unity.
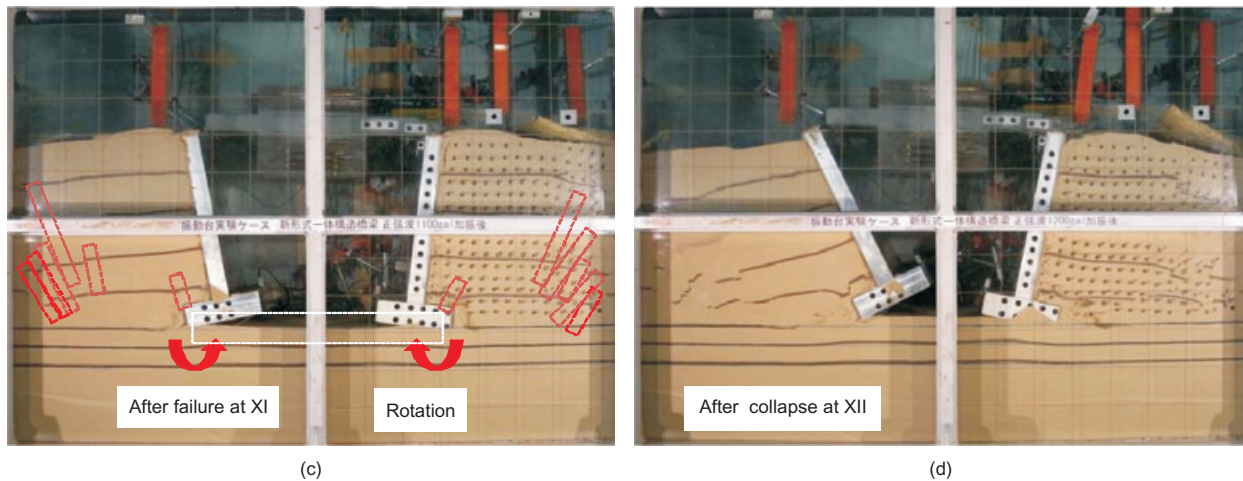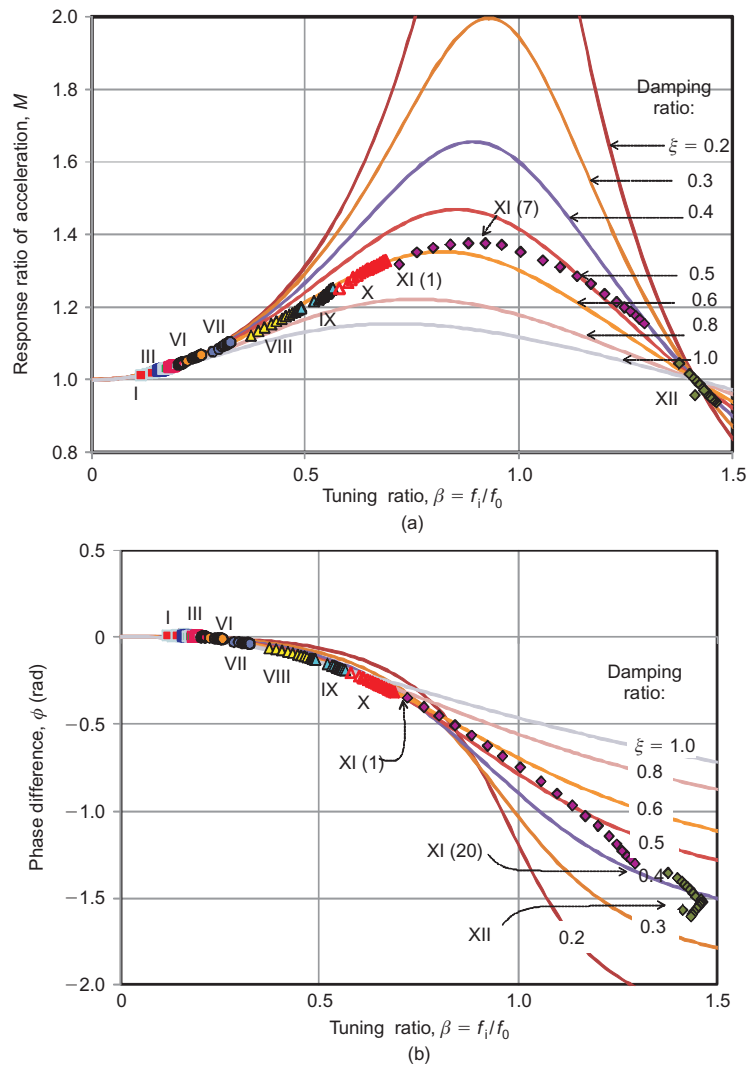
At stage XI (where the resonance state was reached),

Figure 14. Performance of GRS-IB for $f_i = 5$ Hz at all stages: (a) M against β; (b) ϕ against β; (c) deformations observed after failure; (d) deformations observed after collapse
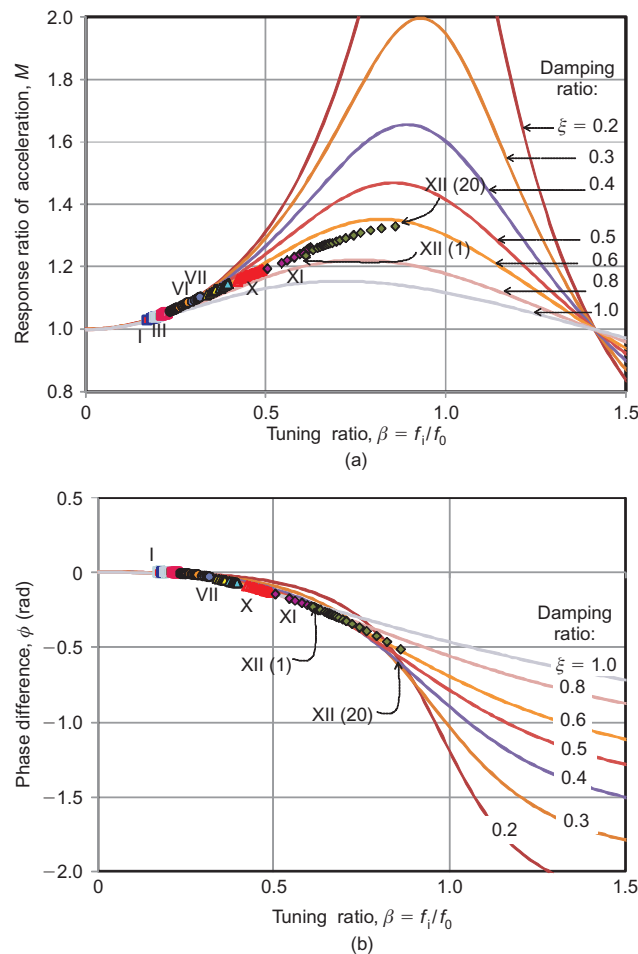
the L-shaped metal fixtures started to yield significantly in flexure, and significant active displacements started at the base of the facings, associated with large rotational movements of the facings about their top. At the same time, the backfill started to settle (Figure 14c). At stage XII (Max[$\ddot{u}_t$] = 1264 gal), β increased towards its final value, 1.46, at state XII(20) (Figure 14a) and the GRS-IB

model collapsed (Figure 14d). That is, the facings rotated severely, the L-shaped metal fixtures yielded significantly, and the bottoms of the facings were largely pushed out, associated with pullout failure of the reinforcement layers and/or connection failure at the back of the facing at the low level of the wall (Hirakawa *et al.* 2007).

5.6. GRS-IB with rectangular prismatic cement-mixed sand zone (GRS-IB-C)

The model started to failing when $\text{Amp}[\ddot{u}_t]_{\text{resonance}} = 1434$ gal and $\beta = \beta_{\text{resonance}} = 0.86$ at stage XII. As for model GRS-IB, the reinforced backfill zone, particularly the cement-mixed sand zone immediately behind the facing, exhibited monolithic behaviour. No shear bands developed inside the cement-mixed zone. As shown later, by arranging a cement-mixed sand zone, the initial stiffness did not increase, but the rate of increase of β was noticeably less (Figure 15a). This trend is due to a decrease in the decreasing rate of the stiffness of the backfill. Correspondingly, the phase difference, ϕ, at the same stage was kept slightly smaller than that for the GRS-IB model (Figure 15b). Moreover, the value of M_{peak} at resonance (at state XII(20)) was equal to 1.33, which was marginally lower than that for the GRS-IB model ($M_{\text{peak}} = 1.38$). This trend indicates that the damping ratio at resonance marginally increased with an increase in the degree of structural integration by arranging a cement-mixed sand zone immediately behind the facing.

The failure mode of the GRS-IB-C model was very similar to that of the GRS-IB model, except that only slight shear bands were formed in the unreinforced backfill zone back of the cement-mixed sand zone. This is because the rectangular prismatic zone of cement-mixed silica sand prevented excessive yielding of the L-shaped fixtures. This kept the stiffness of the bridge system higher, and made the system more ductile (i.e. a lower rate increase of β) than the GRS-IB model. As a result, the settlement at the crest of the backfill behind the facing and its rate of increase were kept markedly smaller.

5.7. GRS-IB with trapezoidal cement-mixed sand zone (GRS-IB-C-T)

This bridge model exhibited the highest strength against failure among the tested bridge models. That is, when $\text{Amp}[\ddot{u}_t]_{\text{resonance}} = 1,502$ gal and $\beta = \beta_{\text{resonance}} = 0.92$ at stage XIII (Figures 16a and 16b), this model started to fail: the L-shaped metal fixtures started to yield, moderately, and the abutments started to rotate forwards about the top, also moderately. The failure mode of this model is very similar to that of the GRS-IB-C, but the trapezoidal cement-mixed sand zone together with the facings behaved highly monolithically in a very stable manner. This trend can be attributed to the trapezoidal shape of the cement-mixed sand zone as well as the high connection strength of the reinforcement layers at the back of the facings and the high adherence of the embedded reinforcements to the cement-mixed sand zone. As a result, excessive yielding of the L-shaped fixtures was restrained, and shear bands developed only slightly at relatively

Figure 15. Performance of GRS-IB-C for $f_i = 5$ Hz at all stages: (a) M against β; (b) ϕ against β
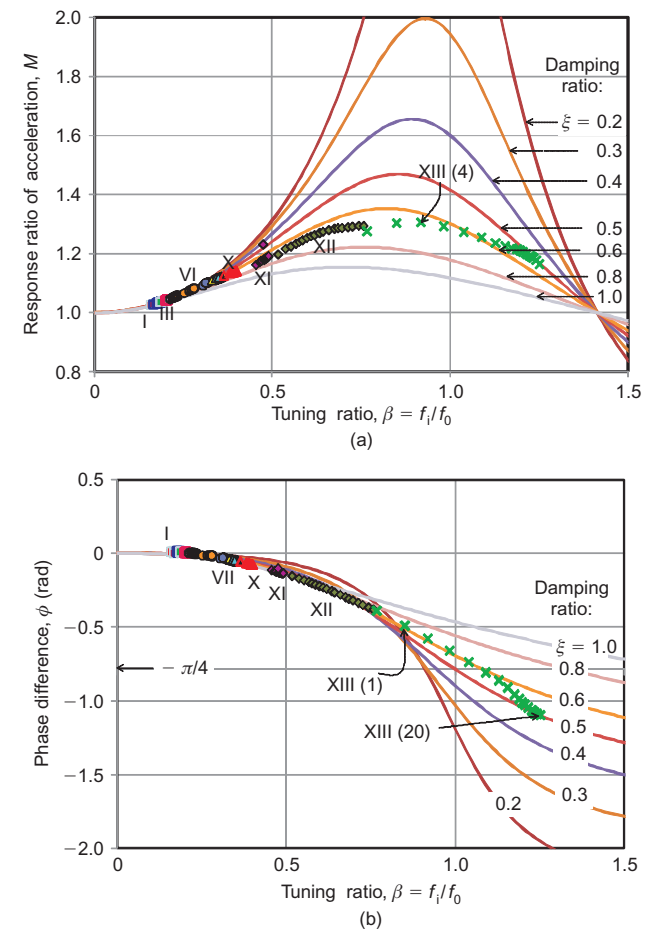
Figure 16. Performance of GRS-IB-C-T for $f_i = 5$ Hz at all stages: (a) M against β; (b) ϕ against β

greater distances from the facings in the unreinforced backfill zone and the supporting ground below the footing foundation. At the same time, settlement of the backfill behind the facing was kept small. These trends of behaviour are all better than for the GRS-IB-C model. They are reflected in the lowest value of β at the same loading stage and the lowest rate of increase of β among all the models examined. Moreover, the value of M_{peak} at resonance (at state XIII(4)) was equal to 1.31, which was the lowest, indicating that this model has the highest damping capacity of this model, probably due to the highest degree of structural integration.

6. EVALUATION OF DYNAMIC STABILITY

6.1. Strength

Figure 17 compares the response acceleration at the girder, $\text{Amp}[\ddot{u}_t]_{resonance}$ (i.e. the strength) and the base accelerations at resonance, $\text{Amp}[\ddot{u}_b]_{resonance}$, at which failure started to occur, for all the bridge models (Table 1). For reference, the maximum base accelerations, $Max[\ddot{u}_b]$, at the stage when resonance occurred are also plotted. It may be seen that the strength increases consistently by reinforcing the backfill (while using bearings), by integrating the girder to the facings (with unreinforced backfill), by integrating the girder to the facings and reinforcing the backfill, and by cement-mixing part of the backfill immediately behind the facing (in particular in a trapezoidal shape) for the GRS integral bridge. Among the increases in the strength, that achieved by reinforcing the backfill of the IB model is the largest.

6.2. Initial stiffness and softening rate

With an increase in the amplitude of the base acceleration at $f_i = 5$ Hz, stage by stage, the failure state was reached after the stiffness of the components constituting the respective bridge models had decreased at an increasing rate (i.e. initially gradually, then fast): that is, after β had increased at an increasing rate. When the failure state started, the decreasing rate of the bridge stiffness was
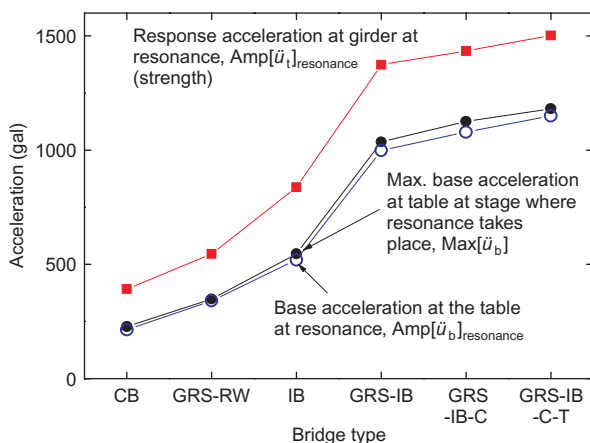
further accelerated, which continued until the ultimate collapse state was reached. These observations indicate that the following three measures are effective in keeping the dynamic behaviour of a given bridge system far away from the resonance state:

1. increasing the initial stiffness of a bridge system (i.e. increasing the initial natural frequency, f_0), so that the initial value of β, which is smaller than unity, decreases, and the initial response and therefore the initial damage to the system reduces;
2. reducing the decreasing rate of the stiffness of a given bridge and increasing the residual stiffness after large deformation, so that the rate of increase of β decreases, keeping the value of M smaller and slowing down the process to failure;
3. increasing the damping capacity, particularly at failure, to reduce the value of M at resonance.

To show that these three measures can be achieved by better integration of the components of a given bridge system (i.e. the girder, the facings and part of the backfill and the supporting ground), the dynamic characteristics of three models (CB, GRS-RW and GRS-IB) are compared in Figure 18. Figure 18a shows the increase in β (i.e. decreasing stiffness) with an increase in the base acceleration, $\text{Amp}[\ddot{u}_b]$. Figure 18b shows the decrease of the natural frequency f_0 (i.e. $f_i = 5$ Hz divided by the β values shown in Figure 18a). Figure 18c shows the increase of the acceleration response ratio M. The following trends of changes in the dynamic behaviour, all associated with an increase in the degree of integration of the components of bridge, may be seen from these figures.

1. The initial f_0 values, observed immediately after the start of state I, increased markedly from 11 Hz (CB) to 24 Hz (GRS-RW), and then to 35 Hz (GRS-IB), which resulted in a marked decrease in the initial value of $\beta = f_i/f_0$ from 0.48 (CB) to 0.21 (GRS-RW), and then to 0.15 (GRS-IB).
2. With the CB model, failure was reached most rapidly for the lowest base acceleration, showing that the failure of this model was the most brittle. By contrast, with the GRS-IB model, the failure stage was approached more slowly: the failure was more ductile. The behaviour of GRS-RW bridge model was intermediate between these two.
3. The value of M_{peak} at resonance decreased, associated with an increase in the initial f_0 value and a decrease in the brittleness.

To evaluate the advantages of tensile-reinforcement of the backfill, and further cement-mixing of part of the backfill, the dynamic behaviour of four integral bridge models (IB, GRS-IB, GRS-IB-C and GRS-IB-C-T) are compared in Figure 19, in similar fashion to Figure 18. It may be seen from Figures 19a and 19b that the initial β values of the four models are similar, at about $0.14 - 0.2$. This fact shows that measure 1 (stabilising the backfill with tensile-reinforcement and cement-mixing) did not
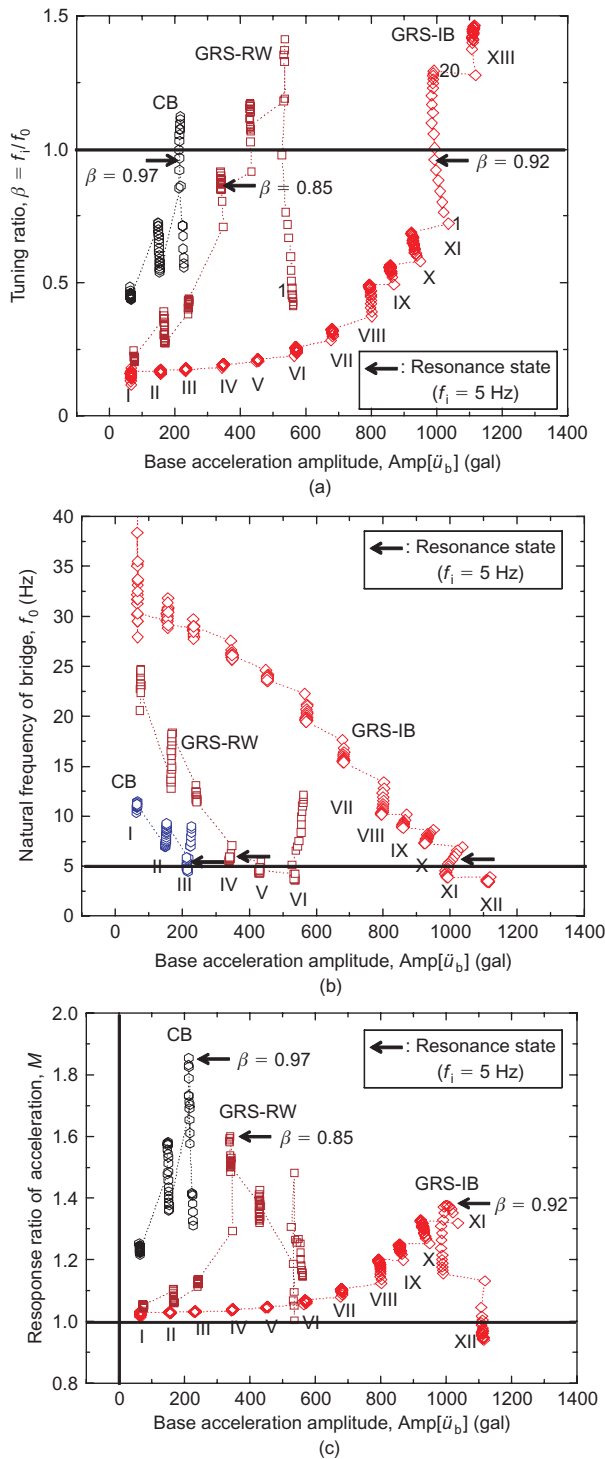

Figure 17. Dynamic strengths of all bridge types for $f_i = 5$ Hz at all stages

Figure 18. Relationships between (a) β, (b) f_0, (c) M and Amp[$\ddot{u}_b$] for bridge models CB, GRS-RW and GRS-IB
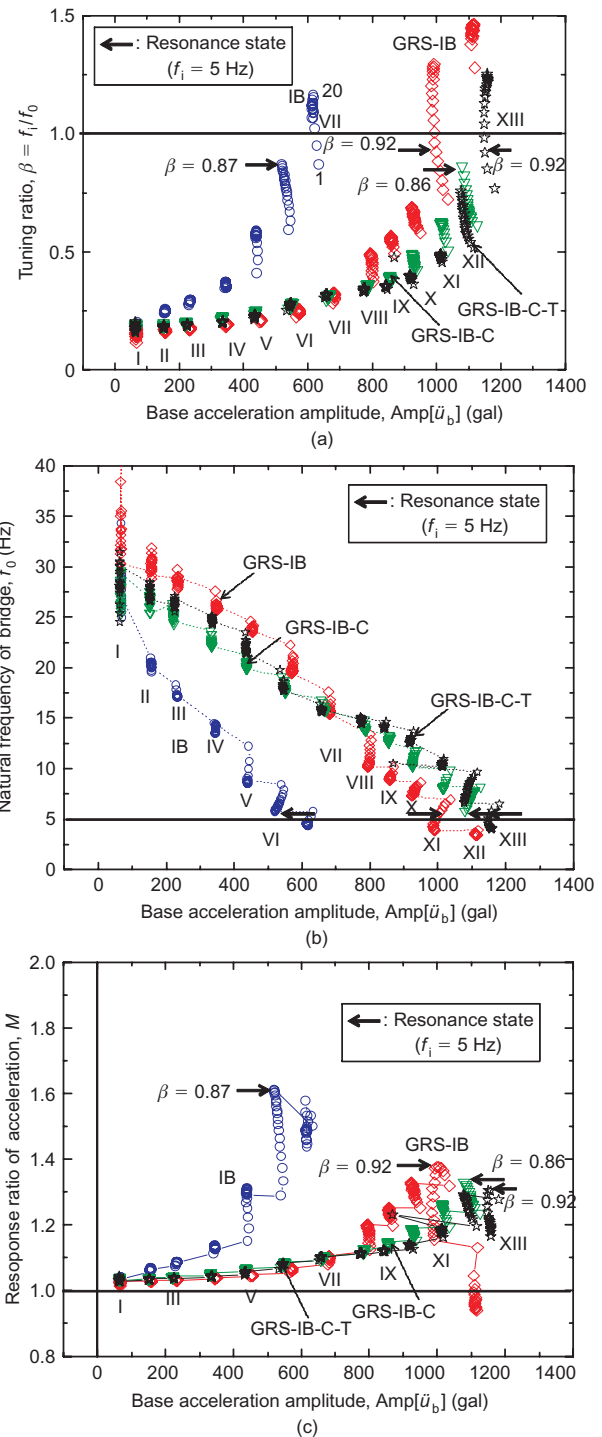

Figure 19. Relationships between (a) β, (b) f_0, (c) M and Amp[$\ddot{u}_b$] for integral bridge models GRS-IG, GRS-IB-C and GRS-IB-C-T

work very effectively. On the other hand, the rate of increase of β towards a value at resonance, $\beta_{resonance}$ (i.e. the rate of decrease of f_0 from about $25-35$ Hz towards $f_i = 5$ Hz) with an increase in the input acceleration decreased considerably with tensile-reinforcement of the backfill, and decreased further with cement-mixing. The same trend can be seen in the process after failure (at resonance) towards collapse. This result indicates that measure 2, with tensile-reinforcement and cement-mixing of the backfill the backfill, is very effective. As a whole,

the dynamic ductility increases, from CB (the smallest), to GRS-RW, IB, GRS-IB, GRS-IB-C and GRS-IB-C-T.

6.3. Magnification ratio and damping at resonance

Among all the bridge models, the CB model exhibited the highest magnification ratio M_{peak} (i.e. 1.85), and the GRS-IB-C-T model exhibited the lowest (i.e. 1.31). The different values of M_{peak} among the different bridge models can be attributed to the different capacities of energy dissipation, represented by the damping ratio, ξ, as an SDOF

system at failure, which is lowest with CB (0.33) and highest with GRS-IB-C-T (0.64) (Table 1). These different ξ values are due to the fact that the components of the CB model (the girder, the abutments and part of the backfill and the supporting ground) are least integrated, and those of the GRS-IB-C-T model are the best integrated. Figure 20 shows the ξ values at failure of the six models. The value increases with an increase in the dynamic strength of the bridge system: that is, in the order CB, GRS-RW, IB, GRS-IB, GRS-IB-C and GRS-IB-C-T. This indicates that measure 3, by integrating the girder to the abutments, tensile-reinforcing the backfill and cement-mixing part of the backfill, is very effective. In the next section, this issue is analysed, referring to the fact that the total capacity of energy dissipation obtained by the SDOF analysis consists of the material damping inside the bridge system and the dissipation damping by wave propagation.

7. ENERGY DISSIPATION CAPACITY

7.1. Damping ratio and shear strain relations

The approximated average shear strain, γ, in the backfill, which controls the material damping of the backfill, was obtained as $\gamma = \tan \theta$, where θ is the tilt angle of the facing (Figure 21a), for all models except the GRS-RW model. For GRS-RW, the shear strain was obtained from the rotation angle θ of the sill beam supporting the girder via a fixed shoe. The shear strain, γ, comprises the average shear strain, γ_{ave}, and the cyclic shear strain, γ_{cyc}.

Figures 21b and 21c show the relationships between the damping ratio ξ and γ_{cyc} obtained by SDOF analysis of the six models. As seen from Figures 12a and 12b, the ξ values of the GRS-RW model are most erratic among the bridge models examined. This trend is probably due to the fact that the sill beams are not unified to both facings and girder: therefore, the dynamic deformation mode of the bridge system deviates most from that illustrated in Figure 9, for which SDOF system modelling is appropriate. Moreover, the definition of shear strain (Figure 21a) is least relevant for the GRS-RW bridge model. In Figure
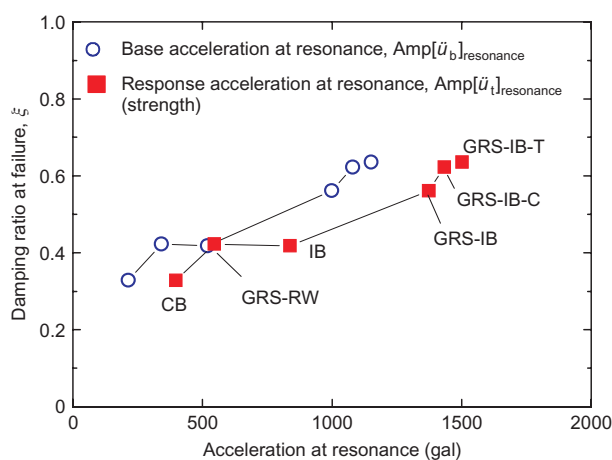
21b, therefore, for the GRS-RW model, only the ξ-γ_{cyc} relations at stages IV and V (at failure and immediately after) are presented. With the other models, the relations are presented at all stages, except for those at the very beginning at the respective stages of shaking, where the back-calculated values of ξ are not accurate.

In these figures, two other relationships between the material damping and γ_{cyc} of Toyoura sand are presented. The first is that obtained by substituting a confining pressure equal to 3.4 kPa and a void ratio of 0.70 into an empirical equation for the values at the 10th loading cycle obtained by cyclic torsional shear tests performed on Toyoura sand at a loading frequency of 0.1 Hz (Tatsuoka *et al.* 1978). The confining pressure (3.4 kPa) is the mean principal stress at the mid-depth of the backfill (i.e. 22.5 cm) when the horizontal stress is equal to the vertical stress. The void ratio (0.70) is the value that may be reached after many large cyclic shear deformations exhibiting a strong trend of dilatation. As these values are only a rough estimate, and as the range of confining pressures employed in the torsional shear tests was 24.5–196 kPa, the torsional shear test relation should be considered as a reference for the first approximation.

The second relation is that obtained from time histories of shear stress and shear strain at a single representative point in the backfill of the IB model, evaluated by the back-calculation method proposed by Zeghal and Elgamal (1994), Zeghal *et al.* (1995a, 1995b) and Brennan *et al.* (2005). To this end, records of a set of accelerometers arranged vertically in the backfill (A17, A10, A7 and A4 together with the extrapolated acceleration record at the free surface, A0; Figure 4a) were selected. The representative point where all the analysis was concentrated was point A7. The horizontal displacement at the respective accelerometers was back-calculated from its acceleration record by a double integration method. In so doing, the result was filtered using a fourth-order Butterworth filtering procedure with a bandpass of 0.1–25 Hz while using a linear baseline correction. The relationships between the damping ratio and shear modulus at the 10th cyclic of loading and γ_{cyc} are plotted in Figures 21b and 21c.

The following trends may be seen from Figures 21b and 21c. First, in the seismic design of ordinary reinforced concrete (RC) structures, a relatively low damping ratio ξ at failure (about 0.05) is assumed, whereas $\xi = 0.2$ may be assumed for very severely damaged conditions. With the four types of integral bridge model, however, the value of ξ became much higher than 0.2 long before the failure state was reached (Figures 21b and 21c), and the value at failure was much larger (Figure 20), both resulting in relative low dynamic responses before and at failure. This advantageous feature is due mainly to very high material damping attainable in the backfill and supporting ground inside and outside the various bridge systems (as SDOF systems).

Second, the two ξ and γ_{cyc} relations from cyclic torsional shear tests and stress−strain analysis of the backfill in the shaking-table test on the IB model are not very close to each other. A noticeable difference between the two relations could be due to several factors, including
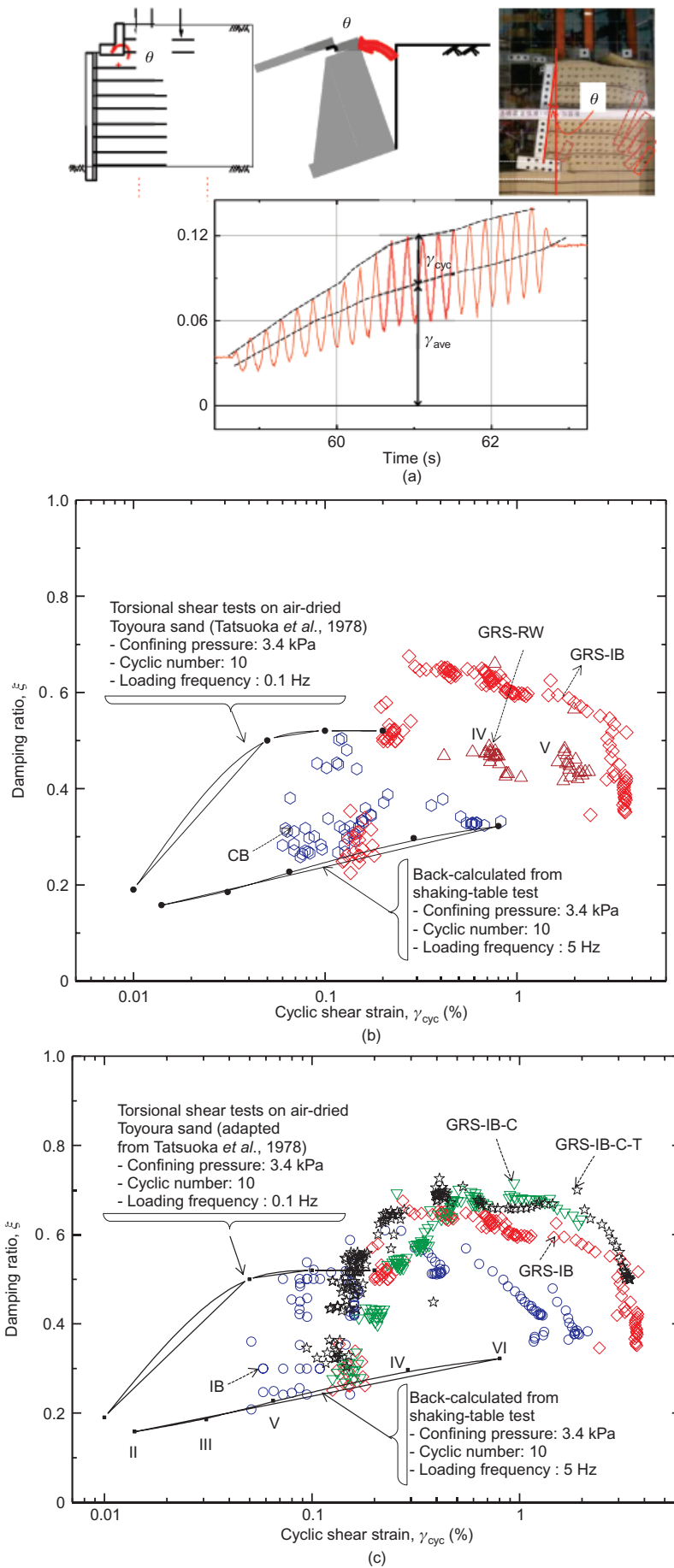

Figure 20. Relationship between damping ratio ξ and base acceleration at resonance for all models. A single value of ξ is presented for all models

Figure 21. (a) Definition of backfill shear strain $\gamma = \tan\theta$; (b), (c) ξ and γ_{cyc} relations from SDOF analysis of shaking-table test results compared with results from stress–strain analysis of shaking-table test on IB model and from torsional shear tests

different loading frequencies (5 Hz and 0.1 Hz) and the various approximations used. More study is necessary to evaluate this, but the trends of non-linear behaviour are broadly similar.

Third, with all the bridge models other than the GRS-RW model, the values of ξ values obtained by SODF analysis increase very rapidly with γ_{cyc} until a specific stage is reached. This trend is not largely different from the two relations representing the material damping. However, the values of ξ from the SDOF analysis tend to exceed the material damping, and in some cases they become larger than the possible maximum value of the material damping, equal to $2/\pi$, for rigid-perfectly plastic stress–strain behaviour. Furthermore, it is not likely that all the dynamic energy of a bridge model is consumed inside the assumed SDOF system. The relationship between the values of ξ from the SDOF analysis and the material damping is complicated. However, it is likely from the above that the values of ξ obtained by the SDOF analysis include dissipation damping by wave propagation in addition to the material damping consumed inside the system. This inference is supported by the trend that, after having exhibited a maximum value, the values of ξ from the SDOF analysis obviously start to decrease with a continuous increase in γ_{cyc}, unlike the behaviour of the material damping. This trend probably occurs because the energy dissipation rate became smaller with an increase in the degree of the disintegration of the components of the model (i.e. the girder, the abutments and part of the backfill and the supporting ground) with an increase in γ_{cyc}, associated with an increase in the deformation of the model.

7.2. Energy dissipation

The following trends of behaviour, which support the inference described above, may be seen from Figures 21b and 21c. First, for the CB model, the maximum value of ξ from the SDOF analysis is the lest, which means that this model has the lowest capacity for energy dissipation by material damping and wave propagation, because it has the least degree of structural integration. Second, the ξ–γ_{cyc} relations of the four types of integral bridge model (IB, GRS-IB, GRS-IB-C and GRS-IB-C-T) are consistent. That is, with the IB model, after having exhibited a peak value at stage V, ξ gradually decreased with increase in γ_{cyc} until the failure state was reached. This trend continued until the collapse state was reached. This trend is probably due to: separation between the facing and the backfill caused by large displacements of the facings, as well as large deformation and settlement of the backfill; and a decrease in the coefficient of vertical and lateral subgrade reaction at the facing, and a loss of contact between the base of the facing bottom and the supporting ground. In comparison, with the GRS-IB, GRS-IB-C and GRS-IB-C-T models, ξ did not start to decrease before failure was reached. Also, the decrease in ξ with γ_{cyc} after failure was smaller than for the IB model, particularly smaller for the GRS-IB-C and GRS-IB-C-T models. This trend is probably due to less disintegration of the compo-

nents of bridge, obtained by cement-mixing part of the backfill immediately behind the facing.

It was attempted to evaluate the energy dissipation by analysing records of a set of accelerometers arranged horizontally in the backfill in the test on the IB model (A6, A7 and A8 in Figure 4a). This is because the deformation mode in the backfill in this test is the most simple shear-like among the six models. Figure 22a shows histories of the acceleration response ratio M at these places in this test. Figure 22b shows histories of the phase difference ϕ between the acceleration records fitted by sinusoidal waves at these different places and the input motion. It was very difficult to evaluate energy dissipation by wave propagation from these test results; yet it may be seen that, except for the initial stage (I, II and III), at any moment only a small part of the backfill adjacent to the facings (i.e. A6 and A7) dynamically displaced in essentially the same phase and magnitude as the facing at the same level (i.e. A15). This indicates that part of the dynamic energy of the girder and facings is transmitted into and consumed in the backfill zone outside the bridge system modelled as an SDOF system. That is, the back-calculated damping ratio ξ of the various bridge models, modelled as SDOF systems, consists of the internal mater-
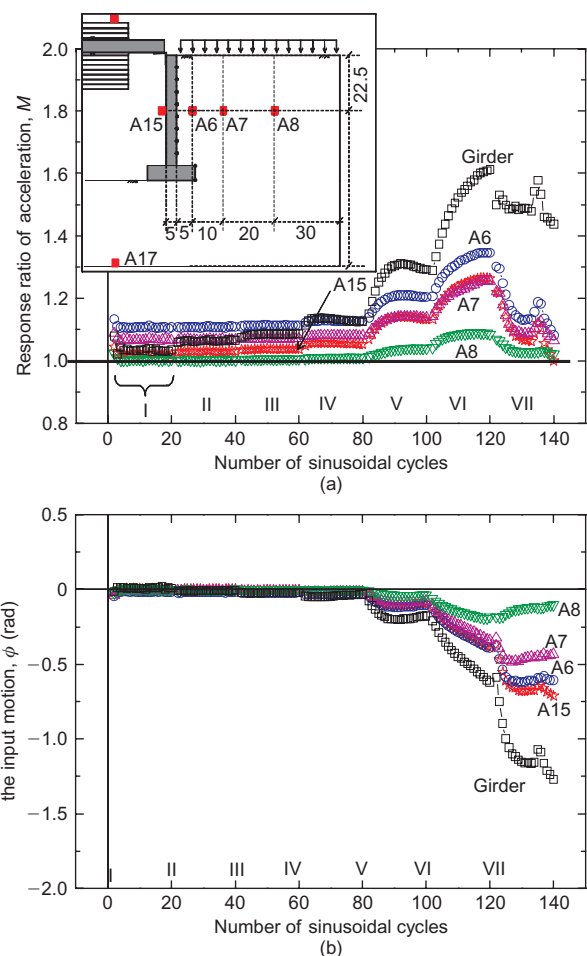
Figure 22. Histories of (a) *M* and (b) *φ* at various horizontal points in backfill for IB model: I, II, III, etc., represent loading stages

ial damping of the system and the dissipation damping by wave propagation.

# 8. DYNAMIC PERFORMANCE UNDER A WIDE RANGE OF FREQUENCY

Figures 23a and 23b show, respectively, the time history of the base acceleration applied at the shaking table consisting of a wide range of frequency, f_i, and its response at the girder from a test on the GRS-IB-C-T-f model. Table 2 shows details of the frequency components at each loading stage. Figure 24a shows the relationships between the applied base acceleration and the response acceleration at the girder in the course of shaking of the GRS-IB-C-T-f model, in which the base acceleration generally increased while changing the input frequency stage by stage (Figure 23a). These relations are compared with that from the test on the GRS-IB-C-T model ($f_i = 5$ Hz). Figure 24b shows the relationships between the response acceleration at the girder and the back-calculated tuning ratio from these two tests. Among the results for a wide range of f_i, the average relation is denoted by a broken curve only for $f_i = 20$ Hz.

In both Figures 24a and 24b, the relations at different stages where different base accelerations were applied at $f_i = 5$ Hz in the tests on GRS-IB-C-T-f model are similar to that from the test on the GRS-IB-C-T model, in which the base acceleration was increased stage by stage, with f_i always equal to 5 Hz. This means that the effects, if any, of intermediate loading histories on the relation for the

Table 2 Input frequencies f_i in test on GRS-IB-C-T-f model.

Stage	f_i (Hz)
I	5
II	10
III	20
IV	2
V	2–3[a], 5, 10, 15, 20, 25, 30
VI	5
VII	2–3, 5, 10, 15, 20, 25, 30
VIII	5
IX	5
X	10
XI	20
XII	2
XIII	5
XIV	2–3, 5, 10, 15, 20, 25, 30
XV–XXIII	5

[a]f_i varied in a range between 2 Hz and 3 Hz. This test is denoted as $f_i = 2$ Hz hereafter.

(a)

(b)
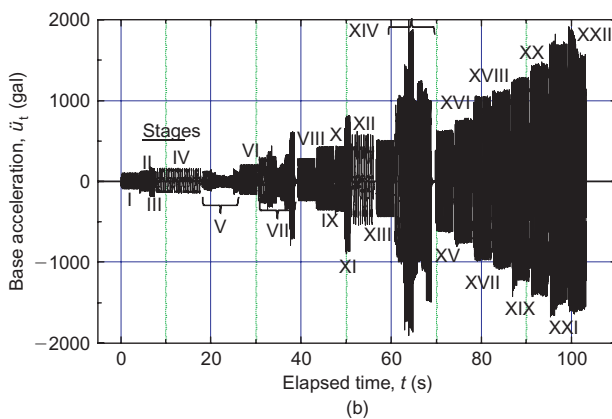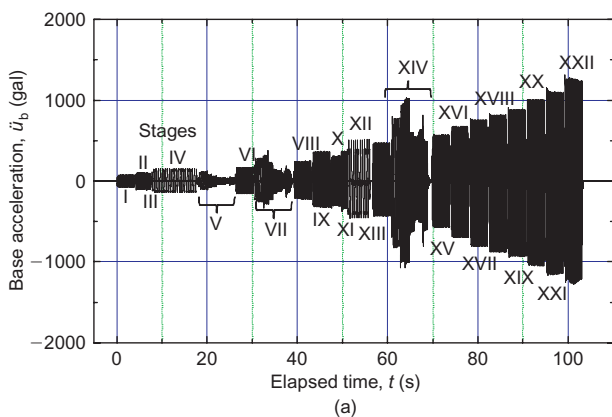
Figure 23. Time histories of (a) base acceleration and (b) response acceleration at girder of GRS-IB-C-T-f model

(a)

(b)
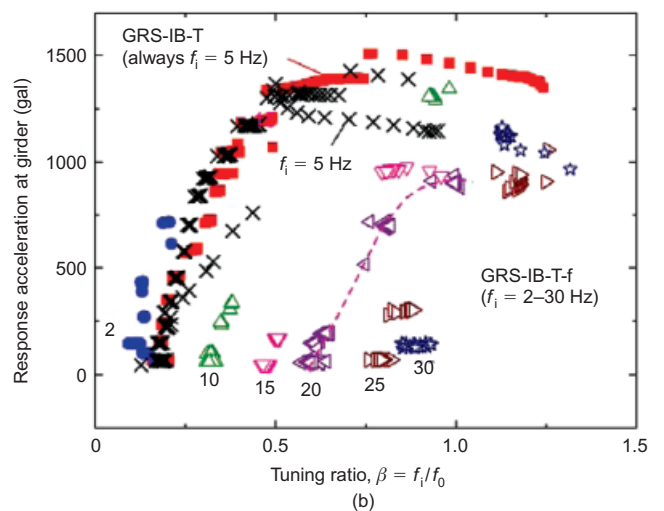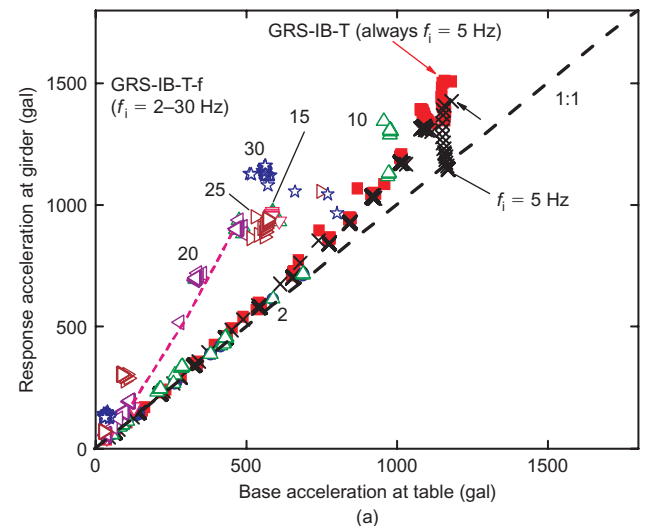
Figure 24. Comparison between GRS-IB-C-T ($f_i = 5$ Hz) and GRS-IB-C-T-f ($f_i = 2, 5, 10, 15, 20, 25$ and 30 Hz): response acceleration at girder against (a) input acceleration at table, (b) tuning ratio

respective f_i values of the GRS-IB-C-T-f model are not significant. If these loading history effects are ignored, the following trends can be seen. In Figure 24a, the response acceleration deviates from the table acceleration earlier at a higher f_i. Correspondingly, in Figure 24b, the relationship between response acceleration and tuning ratio β moves rightwards with an increase in f_i (i.e. an increase in β). As the value of β approaches unity, the resonance state is approached. The response acceleration then tends to exhibit the peak value associated with an increase in the table acceleration, and as a result the magnification ratio, M, exhibits the peak value at resonance. Consequently, with an increase in f_i, resonance occurs earlier (i.e. at a lower table acceleration) and the peak value of the response acceleration decreases in the course of shaking

increasing the base acceleration, resulting in a lower possibility of failure. In the present case, the response acceleration at resonance became largest when f_i was lower than about 10 Hz. These trends are examined in more detail below.

Figures 25a–25f show the relationships between the measured value of M and the back-calculated value of β, together with the theoretical relations for different values of ξ. The following trends of behaviour may be seen.

1. Until the end of stage XIII (Figures 25a–25d), the base acceleration was relatively low. Therefore the bridge was not seriously damaged, even though the value of M at resonance became very high because of relatively low ξ values (lower than 0.3).
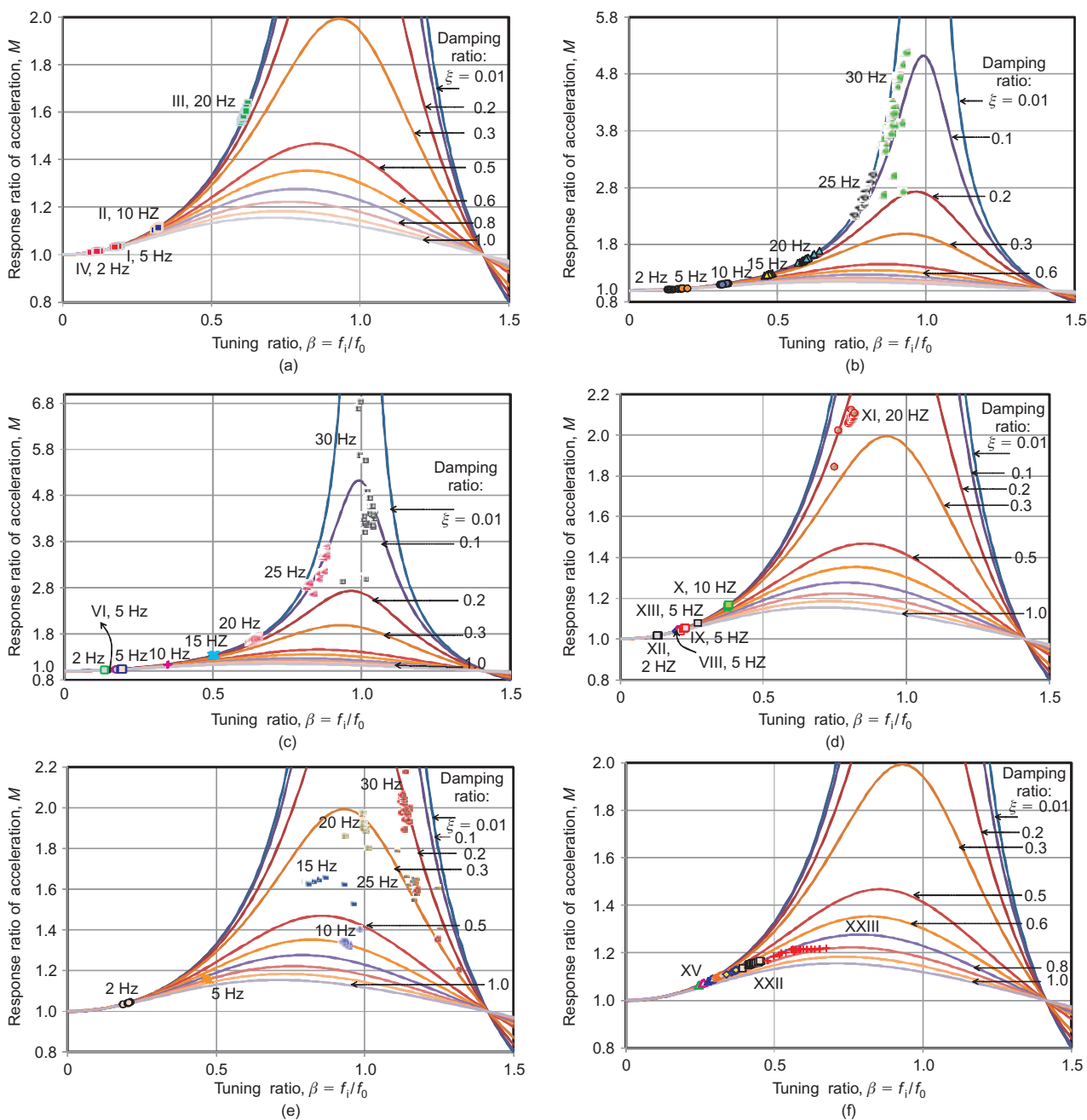

Figure 25. *M* against *β* relations for different *f*ᵢ values for GRS-IB-C-T-*f*: (a) stages I–V; (b) stage V; (c) stages VI–VII; (d) stages VIII and XIII; (e) stage XIV; and (f) stages XV–XXIII

At these stages, the natural frequency f_0 was still kept high, as shown below.

2. At stage XIV (Figure 25e), relatively high base acceleration was applied at a wide range of f_i, but the model did not fail.

3. At stages XV to XXIII (Figure 25f), the base acceleration at $f_i = 5$ Hz increased stepwise until the bridge model failed, as in the other tests.

The dynamic response characteristics when f_i is different from 5 Hz are basically the same as those when $f_i = 5$Hz, but the value of M and the rate of change of β were controlled not only by the base acceleration level but also by the input frequency f_i, as shown below.

In Figure 26, the following data are plotted against the base acceleration for different f_i values observed at all loading stages, irrespective of the order of loading sequence: the value of β (Figure 26a); the natural frequency f_0 ($= f_i/\beta$), where f_i is respective known values and β is the values presented in Figure 26b (Figure 26a); and the value of M (Figures 26c and 26d). Figure 27 shows the relationship between the decay rate, $\Delta f_0/\Delta$Amp[$\ddot{u}_b$], obtained from the slopes of linear relations (with an intersection $f_0 = 35$ Hz when Amp[$\ddot{u}_b$] = 0)
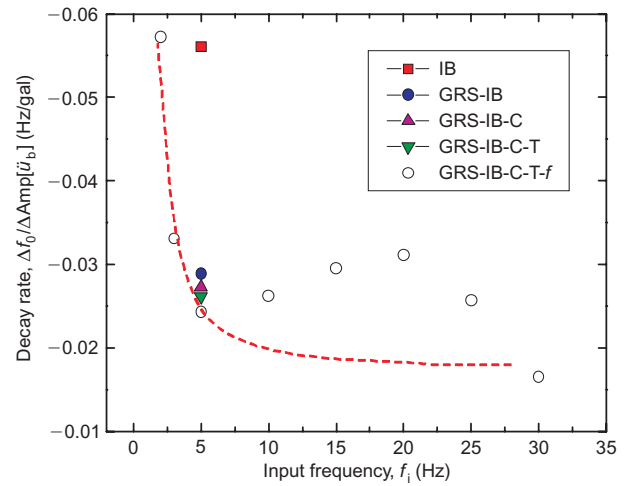

Figure 27. Decay rate of f_0 against input frequency f_i for various integral bridge types

fitted to the respective f_0–Amp[$\ddot{u}_b$] relations plotted in Figures 19b and 26a.

The initial value of f_0 at the very beginning of the test is about 35 Hz (Figure 26a), which is essentially the same as the value for the GRS-IB-C-T model (Figure 19b). The following trends of behaviour may also be seen from Figures 26 and 27.
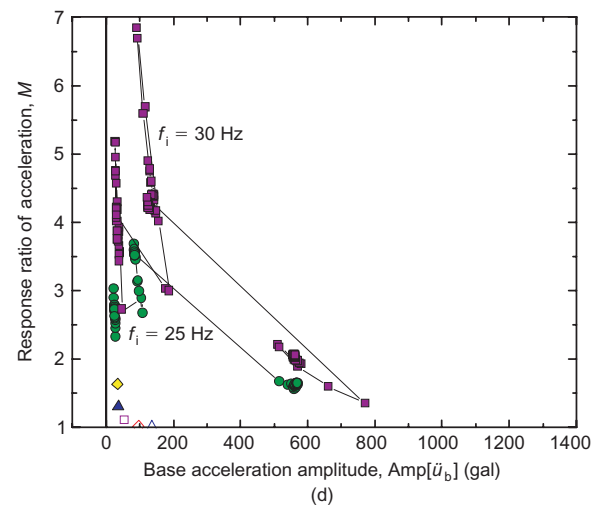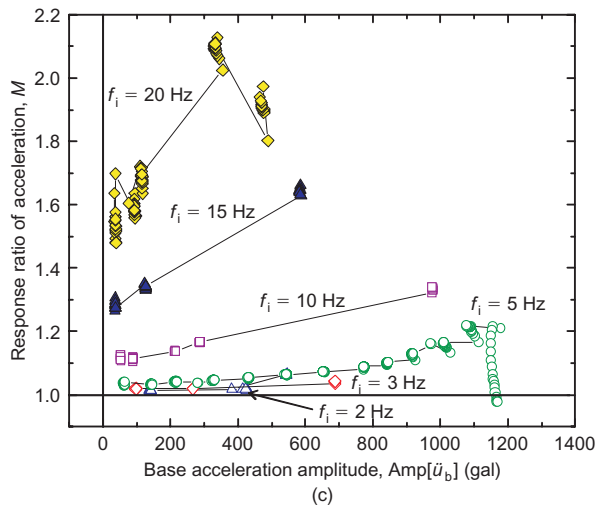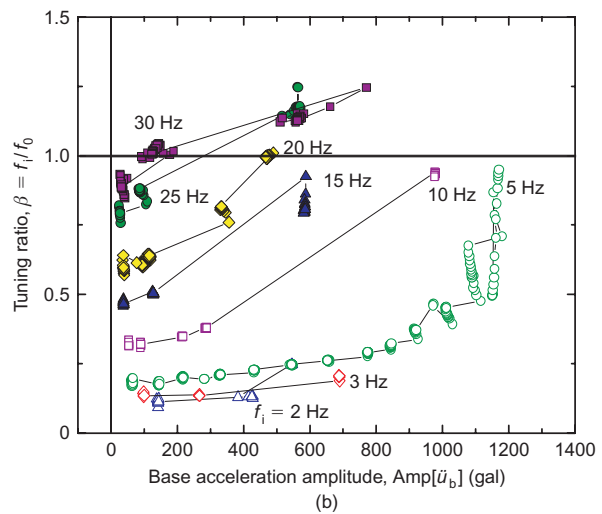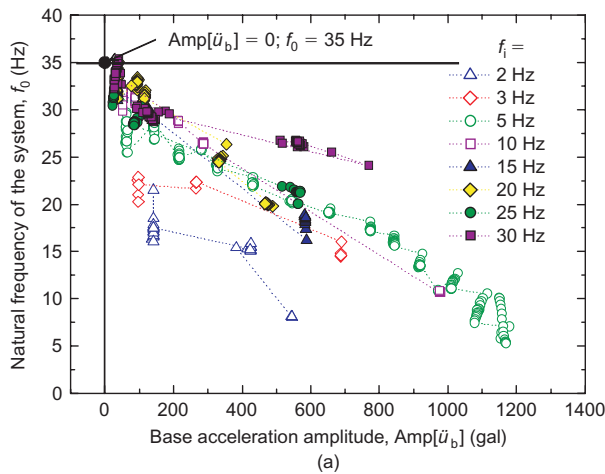

Figure 26. Performance of GRS-IB-C-T-f: relationships between $\ddot{u}_b$ and (a) β; (b) f$_0$; (c), (d) M

1. The rate at which f_0 value with an increase in the base acceleration, $\text{Amp}[\ddot{u}_b]$, generally increased with a decrease in f_i (Figure 26a). This is because, under the same $\text{Amp}[\ddot{u}_b]$ and for the same value of M, the shear strain in the backfill, which is a good index for the damage to the bridge model, increases approximately in proportion to $(1/f_i)^2$. In fact, the decay rate, $\Delta f_0/\Delta\text{Amp}[\ddot{u}_b]$, generally increased with a decrease in f_i (Figure 27). Some irregularity may be seen in the data at $f_i = 15-25$ Hz. This is probably due to the fact that M increased with an increase in f_i because of smaller shear strains, and hence smaller material damping, at these values of f_i. On the other hand, at $f_i = 30$ Hz, the rate of decrease of f_0 with $\text{Amp}[\ddot{u}_b]$ was very low. This is because at a low $\text{Amp}[\ddot{u}_b]$ (about 100 gal), f_0 had already decreased from the initial value (35 Hz) to f_i ($= 30$ Hz), which resulted in resonance. Subsequently, with an increase in $\text{Amp}[\ddot{u}_b]$, the model was subjected to insignificant damage: therefore, it exhibited a small very decrease in f_0 from 30 Hz, to a value close to 25 Hz (Figure 26a).

2. In Figures 26c and 26d, at all f_i values, until a certain limiting value of $\text{Amp}[\ddot{u}_b]$, M continues to increasing with an increase in $\text{Amp}[\ddot{u}_b]$, owing to a continuous increase in β, approaching the value at resonance (a value slightly lower than 1.0). The value of M value then starts to decrease after $\text{Amp}[\ddot{u}_b]$ has reached a certain limit. This limit decreases with an increase in f_i. That is, when f_i is high, this limiting value of $\text{Amp}[\ddot{u}_b]$ is low (i.e. the resonance state is more easily reached). Conversely, when f_i is low, until a high value of $\text{Amp}[\ddot{u}_b]$ value, β increases, although it remains below 1.0, and M continues to increase (i.e. the resonance state is more difficult to reach).

These results show that the damage to a given bridge system is dependent not only on the acceleration level of the input motion, but also on its frequency components. Therefore it is essential to define not only the input acceleration level but also the predominant frequency (i.e. the f_i value) of a given design earthquake motion. That is, when f_i is far below the initial natural frequency f_0, despite a higher decreasing rate of f_0, the resonance state may be reached only after $\text{Amp}[\ddot{u}_b]$ has become very high, owing to the large initial difference between f_0 and f_i. So it is only when strong motion continues at a lower value of f_i that the resonance state may be reached and the bridge may fail. When the f_i value of the input motion is high, and close to the initial natural frequency f_0, a limited extent of damage to the system makes the value of β larger than the value at resonance. In this case, the bridge becomes less likely to fail and collapse. In other words, for a given input motion (i.e. for the same $\text{Amp}[\ddot{u}_b]$ and f_i), the bridge is less likely fail and collapse if the initial value of the natural frequency f_0 is lower than f_i, such that the initial value of $\beta = f_i/f_0$ is higher than the value at resonance (slightly lower than 1.0). In this case, resonance does occur, because β increases from an initial value higher than 1.0 in the course of shaking. However, for ordinary strong earthquake motions, the predominant frequency f_i is of the order of 1–3 Hz. A value of $\beta = f_i/f_0$ higher than 1.0 means a very low initial value of f_0. The resulting structures are too flexible and deformable to be used as bridges for highways and railways, which allow a limited amount of displacement and deformation.

In summary, realistic and effective seismic design of bridges should:

1. make the initial f_0 value as high as possible, compared with the predominant frequency f_i for a given design earthquake motion;
2. make the dynamic ductility as high as possible (i.e. a lower decreasing rate of f_0);
3. make the energy dissipation capacity as high as possible; and
4. make the dynamic strength as high as possible

It is shown above that these advantageous features can be achieved by integrating the girder to the full-height rigid facings while providing tensile reinforcement in the backfill with reinforcing layers connected to the facings, and, if necessary and feasible, by arranging a relevant cement-mixed soil zone immediately behind the facing.

One of the limitations of the model tests presented in this paper is that they are 1g small-scale tests, rather than centrifuge tests. However, owing to the complicated structure of the models used in this study, and the effects of particle size on the behaviour of failing soil (e.g. Tatsuoka *et al.* 1991, 1994; Siddiquee *et al.* 1999; Tatsuoka 2001), it seems that only dynamic centrifuge tests using models of similar size to those used in this study can provide more realistic results. The results from the present study will be a very good reference point for such tests, if performed in the future.

9. CONCLUSIONS

From the results of the experimental and analytical study presented above, the following conclusions can be derived.

1. The GRS-RW bridge, comprising a girder supported by a pair of sill beams via a pair of movable and fixed bearings (i.e. shoes) placed on the crest of geosynthetic-reinforced soil (GRS) retaining walls (RWs) with stage-constructed full-height rigid (FHR) facings is dynamically more stable than the conventional bridge, which comprising a girder supported by abutments via a pair of bearings with unreinforced backfill. However, the GRS-RW bridge is less dynamically stable than the integral bridge, which comprising a girder integrated to a pair of abutments (not using bearings) with unreinforced backfill. This is due to the relatively low dynamic stability of the sill beams and bearings with of GRS-RW bridge, and the high dynamic stability of the integrated girder and facings with the integral bridge.

2. The GRS integral bridge, comprising a girder integrated to the abutments, with the backfill reinforced with geogrid layers connected to the facings, is much more dynamically stable than the

integral bridge. The dynamic stability of the GRS integral bridge can be further increased by arranging a relevant cement-mixed soil zone immediately behind the facing.

3. Analysis of the results of shaking-table tests that treat a bridge system as a damped, single-degree-of-freedom system could capture the main features of the observed dynamic behaviour of the bridge models, although it is approximated.

4. The increase in the seismic stability of bridges by integration of the girder and facings and tensile reinforcement and cement-mixing of the backfill is due to: (a) an increase in the initial value of the natural frequency f_0 to a value much higher than the predominant frequency of the input seismic load; (b) a decrease in the decreasing rate of f_0 during dynamic cyclic loading; (c) an increase in the dynamic energy dissipation capacity, particular when approaching, at and after failure; and (d) an increase in the strength against failure.

NOTATION

Basic SI units are given in parentheses.

f_i frequency of input motion (Hz)
f_0 natural frequency of bridge system (Hz)
M Magnification ratio (i.e. response ratio of acceleration between shaking table and girder) (dimensionless)
M_{peak} maximum value of M (dimensionless)
q_{max} compressive strength of cement-mixed sand (Pa)
$\ddot{u}$ response acceleration at girder relative to base shaking (gal $= 0.01$ m/s^2)
$\ddot{u}_b$ base acceleration at shaking table (gal $= 0.01$ m/s^2)
$\ddot{u}_t$ response acceleration at girder (gal $= 0.01$m/s^2)
Amp$[\ddot{u}_b]$ amplitude of $\ddot{u}_b$ (gal $= 0.01$ m/s^2)
Amp$[\ddot{u}_b]_{resonance}$ amplitude of Amp$[\ddot{u}_b]$ at resonance (gal $= 0.01$ m/s^2)
Amp$[\ddot{u}_t]$ amplitude of $\ddot{u}_t$ (gal $= 0.01$ m/s^2)
Amp$[\ddot{u}_t]_{resonance}$ amplitude of Amp$[\ddot{u}_t]$ at resonance (gal $= 0.01$ m/s^2)

Max$[\ddot{u}_b]$ maximum of Amp$[\ddot{u}_b]$ at stage where resonance occurs (gal $= 0.01$ m/s^2)
Max$[\ddot{u}_t]$ maximum of Amp$[\ddot{u}_t]$ at stage where resonance occurs (gal $= 0.01$ m/s^2)
t elapsed time of shaking (s)
t_c curing time for cement-mixed sand (s)
β tuning ratio ($= f_i/f_0$) (dimensionless)
$\beta_{resonance}$ value of β at resonance (dimensionless)
γ shear strain in backfill (dimensionless)
ξ damping ratio of bridge system as a damped SDOF system (dimensionless)
$\xi_{resonance}$ value of ξ at resonance (dimensionless)
ρ_d dry density of cement-mixed sand (kg/m^3)
ϕ phase difference between input motion and response motion (radians)
ω_0 natural circular frequency of system ($= 2\pi f_0$) (1/s)
ω_i input circular frequency (1/s)

ABBREVIATIONS

CB conventional bridge
FHR full-height rigid facing
GRS geosynthetic-reinforced soil
GRS-RW geosynthetic-reinforced soil-retaining wall
GRS-IB geosynthetic-reinforced soil integral bridge
GRS-IB-C geosynthetic-reinforced soil integral bridge with rectangular prismatic cement-mixed backfill
GRS-IB-C-T geosynthetic-reinforced soil integral bridge with trapezoidal cement-mixed backfill
IB integral bridge
JIS Japanese Industrial Standard
RW retaining wall
SDOF single degree of freedom
TC triaxial compression

REFERENCES

Aizawa, H., Nojiri, M., Hirakawa, D., Nishikiori, H., Tatsuoka, F., Tateyama, M. & Watanabe, K. (2008). Validation of high seismic stability of a new type integral bridge consisting of geosynthetic-reinforced soil walls. *Proceedings of the 5th International Symposium on Earth Reinforcement (IS Kyushu 2007)*, Ochiai. X. *et al.*, Editors, pp. 819–825.

Brennan, A. J., Thusynthan, N. I. & Madabhushi, P. G. (2005). Evaluation of shear modulus and damping in dynamic centrifuge tests. *Journal of Geotechnical and Geoenvironmental Engineering, ASCE*, **131**, No. 12, 1488–1497.

Hirakawa, D., Nojiri, M., Aizawa, H., Nishikiori, H., Tatsuoka, F., Tateyama, M. & Watanabe, K. (2007). Effects of the tensile resistance of reinforcement embedded in the backfill on the seismic stability of GRS integral bridge. *Proceedings of the 5th International Symposium on Earth Reinforcement (IS Kyushu 2007)*, Ochiai. X. *et al.*, Editors, pp. 811–817.

JIS A 1210. (2009). *Test Method for Soil Compaction Using a Rammer*. Japanese Standards Association, Tokyo (in Japanese).

Nishikiori, H. (2007). *Proposal of new bridges reinforcing the backfill and cost-effective rehabilitation of existing bridges*, Master thesis, Department of Civil Engineering, Tokyo University of Science, Japan (in Japanese).

Shinoda, M., Uchimura, T. & Tatsuoka, F. (2003). Improving the dynamic performance of preloaded and prestressed mechanically reinforced backfill by using a ratchet connection. *Soils and Foundations*, **43**, No. 2, 33–54.

Siddiquee, M. S. A., Tanaka, T., Tatsuoka, F., Tani, K. & Morimoto, T. (1999). Numerical simulation of the bearing capacity of strip footing on sand. *Soils and Foundations*, **39**, No. 4, 93–109.

Soma, R., Nishikiori, H., Arita, T., Sakai, S., Tamura, T., Tatsuoka, F., Kiyota, T., Hirakawa, D. & Watanabe, K. (2009). Effects of cement-mixing of geosynthetic-reinforced backfill on the seismic stability of integral bridge. *Geosynthetics Engineering Journal*, **1**, 124–131.

Tatsuoka, F. (2001). Impacts on geotechnical engineering of several recent findings from laboratory stress–strain tests on geomaterials. *Geotechnics for Roads, Rail Tracks and Earth Structures*, Correia, X. & Brandle, X., Editors, Balkema, pp. 69–140.

Tatsuoka, F., Iwasaki, T. & Takagi, Y. (1978). Hysteretic damping of sands under cyclic loading and its relation to shear modulus. *Soils and Foundations*, **18**, No. 2, 25–40.

Tatsuoka, F., Okahara, M., Tanaka, T., Tani, K., Morimoto, T. & Siddiquee, M. S. A. (1991). Progressive failure and particle size effect in bearing capacity of a footing on sand. *Proceedings of the ASCE Geotechnical Engineering Congress, 1991*, Boulder, ASCE Geotechnical Special Publication No. 27, pp. 788–802.

Tatsuoka, F., Siddiquee, M. S. A. & Tanaka,T. (1994). Link among design, model tests, theories and sand properties in bearing capacity of footing on sand, panel discussion. *Proceedings of the 13th International Conference on Soil Mechanics and Foundation Engineering*, New Delhi, Vol. 13, pp. 7–88.

Tatsuoka, F., Tateyama, M., Aoki, H. & Watanabe, K. (2005). Bridge abutment made of cement-mixed gravel backfill. *Ground Improvement, Case Histories*, Indradratna, X. & Chu, X., Editors, Elsevier Geo-Engineering Book Series, Vol. 3, pp. 829–873.

Tatsuoka, F., Hirakawa, D., Nojiri, M., Aizawa, H., Nishikiori, H., Soma, R., Tateyama, M. & Watanabe, K. (2009). A new type integral bridge comprising geosynthetic-reinforced soil walls. *Geosynthetics International*, **16**, No. 4, 301–326.

Zeghal, M. & Elgamal, A.-W. (1994). Analysis of site liquefaction using earthquake records. *Journal of Geotechnical Engineering, ASCE*, **120**, No. 6, 996–1017.

Zeghal, M., Elgamal, A.-W. & Tang, H. T. (1995a). Lotung downhole array. I: Evaluation of site dynamic properties: evaluation of soil nonlinear properties. *Journal of Geotechnical Engineering, ASCE*, **121**, No. 4, 350–362.

Zeghal, M., Elgamal, A.-W. & Tang, H. T. (1995b). Lotung downhole array. II: Evaluation of soil nonlinear properties. *Journal of Geotechnical Engineering, ASCE*, **121**, No. 4, 363–378.